AAAS
Advanced Devices & Instrumentation
Volume 2022, Article ID 9765089, 19 pages
https://doi.org/10.34133/2022/9765089

Advanced Devices & Instrumentation
A SCIENCE PARTNER JOURNAL

*Review Article*

# Review on Metasurfaces: An Alternative Approach to Advanced Devices and Instruments

**Xiaoguang Zhao**,[1,2] **Zhenci Sun**,[1,2] **Lingyun Zhang**,[1,2] **Zilun Wang**,[1,2] **Rongbo Xie**,[1,2] **Jiahao Zhao**,[1,2] **Rui You**,[3] **and Zheng You**[1,2]

[1]*Department of Precision Instrument, Tsinghua University, 100084 Beijing, China*
[2]*State Key Laboratory of Precision Testing Technology and Instruments, Tsinghua University, 100084 Beijing, China*
[3]*School of Instrument Science and Opto Electronic Engineering, Beijing Information Science and Technology University, 100016 Beijing, China*

Correspondence should be addressed to Xiaoguang Zhao; zhaoxg@mail.tsinghua.edu.cn, Rui You; yourui@bistu.edu.cn, and Zheng You; yz-dpi@mail.tsinghua.edu.cn

Received 30 March 2022; Accepted 2 August 2022; Published 12 September 2022



This paper reviews the-state-of-the-art of electromagnetic (EM) metasurfaces and emergent applications in advanced integrated devices and instruments from the design method to physical implementation. The design method includes the analytical coupled mode theory model and commonly used building blocks to construct functional metasurfaces. The modeling approach creates a common design basis of metasurface devices for optical beam steering, focusing, modulation, lasing, and detection. The proof of concept of metasurfaces has been established and is translating to practical applications. Previous studies demonstrated promising applications of metasurfaces including but not limited to optical imaging instruments, biochemical sensing devices, and multifunctional microoptoelectromechanical systems (MOEMS). Significant performance improvement of devices and instruments has been achieved due to the implementation of specially tailored metasurfaces. This review provides an alternative for researchers to step forward on the way of advancing devices and instruments by the deployment of metasurfaces.

## 1. Introduction

Metamaterials, consisting of subwavelength unit cells, represent a type of artificially engineered materials with effective properties, including permittivity [1], permeability [2], chirality [3], and other physical properties [4]. In metamaterials, the shape, geometry, and constituent elements of the subwavelength unit cells and the array fashion jointly determine the effective properties of these artificial materials. Ideal metamaterials are the three-dimensional (3D) array of unit cells, exhibiting bulk, effective electromagnetic (EM) responses [5]. However, due to the difficulties in constructing truly 3D metamaterials and the high insertion loss in the bulk metamaterials, the two-dimensional arrays of subwavelength unit cells, namely metasurfaces, have been proposed to efficiently manipulate the propagation of EM waves [6–8]. Following the pioneer work of infrared (IR) metasurfaces [6, 7], emerging interests have been ignited aiming to control the wave propagation across the EM spectrum with ultrathin engineered metasurface devices.

Metasurfaces can be optimized to efficiently manipulate the wavefront by carefully engineering the amplitude and phase response of the meta-atoms through the unit cell structure design. Extraordinary effects, including anomalous deflection and reflection [1, 9], high-efficiency beam focusing [10], polarization conversion [11], and orbital angular momentum (OAM) generation [12, 13], among others [14], have been demonstrated by metasurfaces across the EM spectral from microwave and terahertz to IR and visible regimes. In addition, metasurfaces are capable of generating significant near-field effects by the resonantly local field confinement, thereby initiating giant nonlinearities [15]. The high degrees of freedom in controlling the metasurface properties enable unprecedented functionalities, such as reciprocity breaking in the magnetic-free conditions by using spatial and temporal modulation [16, 17] and unidirectional propagation of EM energy by engineering the distributed loss and gain [18]. These functions have led to breakthroughs in the systems of light detection and ranging

(LiDAR) [19], advanced imaging [20], biological and chemical sensing [21], communication [22, 23], energy management [24, 25], light emission [26, 27], and augmented reality/virtual reality (AR/VR) [28].

Due to the versatile design space to achieve desired optical properties, metasurfaces are increasingly outstanding with the development of micro/nano fabrication, micro/nanoelectromechanical systems (MEMS/NENS), and microsystems. The early metamaterials and metasurfaces were demonstrated in the microwave regime since the well-established printed circuit board (PCB). With the development of micro- and nanotechnologies, the subwavelength unit cells were fabricated and implemented by using advanced micro/nanoscale fabrication techniques, leading to artificially designed metasurfaces, which improved the performance of MEMS, microsystems, and optoelectronic devices. For instance, the large-scale optical metalenses have been developed as the deep ultraviolet (deep-UV) photolithography processes are available [29]. On the other hand, the unique functionalities of metasurfaces, such as perfect absorption, have enabled novel micro/nanodevices, such as near-zero power IR detectors [30], facilitating the development of microsystems. Therefore, the emerging metasurface technique allows us to interact with EM waves in new fashions, enabling microsystems with improved performance and novel functions. The metasurface technique is a potential factor in creating the virtuous circle of advanced microsystem devices and instruments. In this review, we start with fundamental theories of metasurfaces, describing the codesign framework of metasurface devices. Then, we present latest progresses on the integrated metasurface devices and instruments. Finally, we conclude with challenges in metasurface devices and outlook of the future direction.

## 2. Design and Implementation Methods of Metasurfaces

Metasurfaces manipulate the propagation of EM waves, or light, through the engineering of the local amplitude and phase response of each meta-atom, which acts like a subwavelength antenna. The interference of meta-atoms collectively determines the scattering characteristics of the metasurfaces, analogous to a phased-array antenna, enabling a wide design space to achieve various functions, as shown in Figure 1. When designing a metasurface, we first calculate the amplitude and phase responses of meta-atoms with varied parameters at designated frequencies using analytical models and finite element simulation to build a lookup table. Then, the assembly of meta-atoms is designed based on the interactions in the metasurfaces for specific applications. Finally, the full-wave simulation of the metasurface device will be performed to optimize the metasurface by considering the local and nonlocal coupling among meta-atoms.

*2.1. Modelling Metasurfaces.* To achieve full control over the propagation of EM waves, independent manipulation of amplitude and phase responses, as well as the $2\pi$ phase coverage, is desired by varying the design parameters in meta-atoms. The Pancharatnam–Berry (PB) phase is an efficient

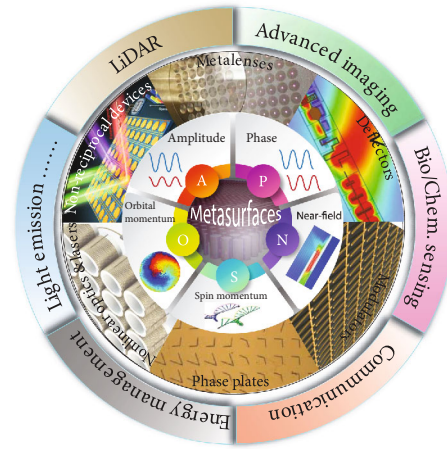


Figure 1: Overview of the functionalities and applications of metasurface devices. Reproduced under the terms of the Creative Commons Attribution license (CC BY 4.0). https://creativecommons.org/licenses/by/4.0/ [13]. Reproduced with permission. Copyright 2019, American Chemical Society [29]. Reproduced with permission. Copyright 2019, Wiley-VCH [31]. Reproduced with permission. Copyright 2019, Wiley-VCH [17]. Reproduced with permission. Copyright 2013, APS physics [32]. Reproduced with permission. Copyright 2018, Wiley-VCH [33].

approach to control the phase response by the inherent geometric phase property in the circularly polarized EM waves, which are widely discussed elsewhere [34]. Another approach to manipulate the phase response is to exploit dispersive, resonance modes of meta-atoms, including the plasmonic resonance [35], dipolar or multipolar resonance [36], and waveguide modes [37]. Owing to the flexibility in dynamically tuning the resonant modes, we focus on the resonance-based metasurfaces in this section.

The resonating behavior of the metasurface may be modeled theoretically by various approaches, including the equivalent circuit model [38], the Lorentz-like effective medium model [39], and the coupled mode theory (CMT) [40]. Among these approaches, CMT provides concise and accurate description on the resonant behavior and unveil the effects of coupling between distinct resonant modes, attracting increasing attentions in the metasurface community.

According to CMT, a single-mode resonator (Figure 2(a)) may be modeled by [41]

$$\frac{da_1}{dt} = (j\omega_{01} - \gamma_1)a_1, \tag{1}$$

in which $a_1$ represents the mode amplitude of the resonant mode, $\omega_{01}$ is the resonant frequency, and $\gamma_1$ is the decay rate due to both intrinsic ($\gamma_0$) and radiative ($\gamma_r$) losses in the resonator. For the excitation with a specific frequency ($\omega$), we can obtain the mode amplitude and transmission/reflection response by solving Equation (1) in the frequency domain [41, 42]. Without loss of generality, we assume $\gamma_1$ to be $0.005 \times \omega_{01}$ and use the normalized frequency difference $d\omega = (\omega - \omega_{01})/\omega_{01}$ in the calculation. As shown in Figure 2(b), the phase of the transmission coefficient is bounded by -90° and 90°, and the amplitude varies significantly due to the

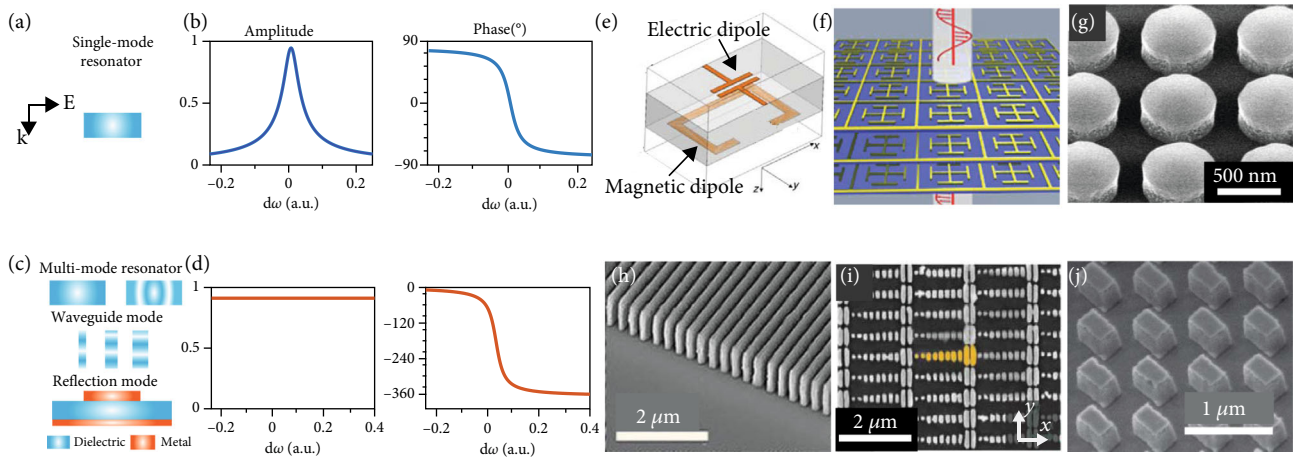


FIGURE 2: The illustration of theoretical modeling and building blocks. The illustration of (a) a single-mode resonator and (b) corresponding response. Illustrations of (c) various approaches to achieve the Huygens' condition and (d) the ideal amplitude and phase response of Huygens' metasurfaces. (e–j) Metasurfaces to achieve the 360° phase coverage by various approaches. (e) Reproduced with permission. Copyright 2013, APS physics [32]. (f) Reproduced with permission. Copyright 2019, Elsevier [50]. (g) Reproduced with permission. Copyright 2013, American Chemical Society [51]. (h) Reproduced with permission. Copyright 2018, Wiley-VCH [37]. (i) Reproduced with permission. Copyright 2012, American Chemical Society [54]. (j) Reproduced with permission. Copyright 2014, American Chemical Society [55].

resonance, indicating that the amplitude and phase of the metasurface are coupled leading to a limited design space.

The limitation of amplitude and phase response may be broken by taking multiple resonators or resonant modes into the systems [42]. Without loss of generality, we may consider a resonator exhibiting two distinct resonant modes (Figure 2(b)), the response of which may be modeled by [43, 44]

$$\frac{d}{dt}\begin{bmatrix} a_1 \\ a_2 \end{bmatrix} = \begin{bmatrix} j\omega_{01} - \gamma_1 & \kappa_{12} \\ \kappa_{21} & j\omega_{02} - \gamma_2 \end{bmatrix}, \tag{2}$$

in which $a_i$ represents the mode amplitude of the resonant modes, $\omega_{0i}$ is the resonant frequency, $\gamma_i$ is the decay rate, and $\kappa_{ij} = \kappa_{ji}$ $(i, j \in \{1, 2\}$ and $i \neq j)$ are the coupling factor between the modes. As shown in Figure 2(c), distinct resonant modes can be achieved by varied approaches, including multipolar resonances, waveguide modes, and the Fabry-Perot mode in the reflection configuration [45]. Herein, waveguide modes refer to the eigenmodes of the meta-atom due to the longitudinal multiple reflections. For a coupled resonator in the ideal condition (two orthogonal modes with matched resonant frequencies and decay rates), a 360° phase coverage may be achieved without amplitude variations [42], as shown in Figure 2(d), allowing it to be a qualified building block of Huygens' metasurfaces. CMT provides a lumped-parameter description of the resonating metasurface and can be exploited to design the unit cell structure through quasinormal modes (QNM) expansion [46].

After obtaining the response of constituent meta-atoms, the overall metasurface array will be designed for various applications. The overall response of a metasurface is governed by Huygens' principle, where every point on a wave front is a source of wavelets emitting waves with the same speed as the source wave to form the new wave front [47]. On the metasurface, waves reflected and transmitted by each meta-atom generate different amplitude modulation and phase shift, thereby leading to an arbitrarily desired wave front due to the interreference effect. The response of the designed meta-atoms and metasurface should be designed and simulated by using numerical approaches, including finite difference time domain (FDTD) simulation, finite element analysis (FEA), and finite integral techniques (FIT) [48]. Recently, inverse design approaches enabled by deep learning attract increasing interests due to the capability of efficiently identifying the global optimal solution for the metasurface design [49].

*2.2. Building Blocks.* Meta-atoms of Huygens' metasurfaces are implemented by metals or dielectrics with judiciously designed geometries, which support coupled modes and generate desired phase distribution for wave front manipulation. In early efforts (Figure 2(e)), the electrical dipoles induced by the cut wires and magnetic dipoles induced by the split ring resonators were combined to generate the 360° phase variations in the transmission to steer the wave front with over 80% efficiency [32]. A similar approach is stacking multiple layers of metasurfaces, as shown in Figure 2(f), to achieve efficient wave manipulation via the collective interlayer mode coupling [50]. In dielectric metasurfaces, the low-loss nanoparticles support both transverse electric (TE) and transverse magnetic (TM) modes governed by Mie resonances, giving rise to the full-range phase coverage when the two modes overlap with each other [51], as shown in Figure 2(g). The amplitude and phase are independently controlled by combining the PB phase and scattering strength control in dielectric metasurfaces [52]. The emerging bound states in the continuum (BIC) provide another paradigm to achieve the Huygens' condition through

controlling the coupling between distinct modes [53]. In addition, high aspect ratio dielectric scatters that support waveguide modes lead to the high-efficiency phase control, even for large incident angles (Figure 2(h)) [37]. These examples demonstrate that meta-atoms possessing multiple modes can serve as building blocks of metasurfaces for transmissive wavefront manipulation.

Metasurfaces can be configured in the reflection mode as well by adding a ground plane at the back of the subwavelength meta-atoms. In the reflection mode, the metasurfaces block the transmitted waves and manipulate the reflected waves. Such metasurfaces are considered a resonator coupled to one port, and the full range of phase coverage may be achieved by tailoring the loss factors [56]. When the intrinsic loss is larger than the radiative loss, meaning that the metasurface is overdamped, the phase of the reflection spectrum may cover the full 360° variations [41]. By tailoring the thickness of the low-loss spacer between the metasurface and the ground plane, the relation between losses may be modified to control the phase response. Both metallic (Figure 2(i)) [54] and dielectric (Figure 2(j)) [55] subwavelength structures serve as the meta-atoms of the high-efficiency reflective metasurfaces. These basic building blocks in either transmission or reflection configurations or their variations form a toolbox, from which the designers may choose and optimize targeting to specific functions and applications.

In addition to manipulating the propagation of EM waves, metasurfaces provide a platform to engineer or enhance the near-field interactions. The metasurface may tailor the effective surface impedance to achieve perfect absorption [57–60] and superabsorption [61], thereby improving the conversion of EM energy to other types of energy, including heat [62] and electric potentials [63]. The electric and magnetic field is confined in the vicinity of subwavelength meta-atoms, arising significant field enhancement with ratios ranging from tens to hundreds of times. Therefore, improved nonlinear response and lasing effects are facilitated by near-field enhancement [14, 31, 64]. Metasurfaces with engineered near-field properties enable the enhanced performance and novel functions of devices and instruments, including MEMS and optoelectronic microsystems [65]. In this review, we mainly focused on the metasurfaces for imaging, bio/chemical sensing, and optoelectromechanical systems. Metasurfaces for other applications, such as wireless communication [66], energy harvesting [67], and thermal management [68], can be found elsewhere.

## 3. Application Cases of Metasurfaces

*3.1. Metasurfaces for Enhancing Imaging Microsystems.* Metasurface lenses (metalenses) are alternative solutions to traditional lenses for integrated imaging instruments due to the small size, low cost, scalability, and compatibility with semiconductor processing technologies [69–75]. In addition, metalenses with great capabilities of EM wave manipulation enable unprecedented functionalities, such as aberration-free focusing, flexible phase profile design, arbitrarily definable focal spots [76], polarization selectivity, dual-polarity operation [77], and ultralarge numerical apertures (NA) [78–81], which open up possibilities for a simplified, miniaturized design of imaging instruments.

Aberration correction of lenses remains a challenge and adds complication to various imaging instruments. Defined by the phenomenon that rays emitted from a point object do not meet all at the same image point, aberrations are simultaneously caused by monochromatic and chromatic effects [82]. When operating at a single wavelength, metalenses are naturally able to perform aberration-free focusing under normal illumination [83], and elementary corrections are needed for their adoption in practical imaging applications requiring a large field-of-view. Methods for monochromatic aberration correction of metalenses include incorporating a curved surface [82] and doublet lens design [84, 85] based on ray tracing analysis, and the former may be impractical due to manufacturing complexities. Arbabi et al. proposed a miniaturized optical planar camera composed of a metalens doublet and an image sensor, featuring a fisheye type photography with an angle-of-view larger than 60° × 60°, a small footprint of $1.6 \times 1.6 \times 1.7$ mm$^3$, and a nearly diffraction-limited resolution, operating at the wavelength of 850 nm [84], as shown in Figure 3(a). Further miniaturization of the camera and the potential for multicolor and hyperspectral imaging will be enabled by doublets designed for different frequencies and fabricated side by side on a single chip.

Metasurfaces are capable of mitigating the chromatic abbreviation through the flexible phase profile design. Apochromatic or superachromatic lenses typically refer to lenses that are corrected for chromatic aberrations at three or four wavelengths, respectively. Unlike their traditional counterparts, metalenses suffer from large phase dispersion. However, judiciously designed metalenses provide an achromatic performance at not only several discretized wavelengths [86–88] but also a continuous bandwidth [89–91] with a single layer of metasurface, as well as a metalens-cascading method [92]. Due to the lack of phase dispersion compensation capabilities, simultaneously achieving a large numerical aperture, polarization-insensitive operation, and broadband achromatic focusing remains a great challenge. The integration of a bandpass color filter and a multiwavelength achromatic metalens may be a practical solution, as shown in Figure 3(b). Red-green-blue (RGB) light beams were selected after the broadband incident light passing through a bandpass filter composed of distributed Bragg reflectors (DBRs) and defect dielectric layers deposited on the backside of the substrate, and then deflected to the same focal spot by the metalens fabricated on the front side [93]. Moreover, simultaneously correcting monochromatic and chromatic aberrations is critical for practical applications, and doublet metalens design has been theoretically demonstrated as an efficient approach [94]. In the midinfrared regime, Ou et al. proposed an implementation scheme of broadband and achromatic metasurfaces based on the birefringent silicon nanopillars to achieve polarization-sensitive/insensitive varifocal metalens and optical vortex generation in the midinfrared regimes [95, 96]. The principle incorporating the Jones matrix in the metasurface phase profile design represents a general approach to enable broadband and arbitrary optical beam manipulation for the imaging and detection applications.

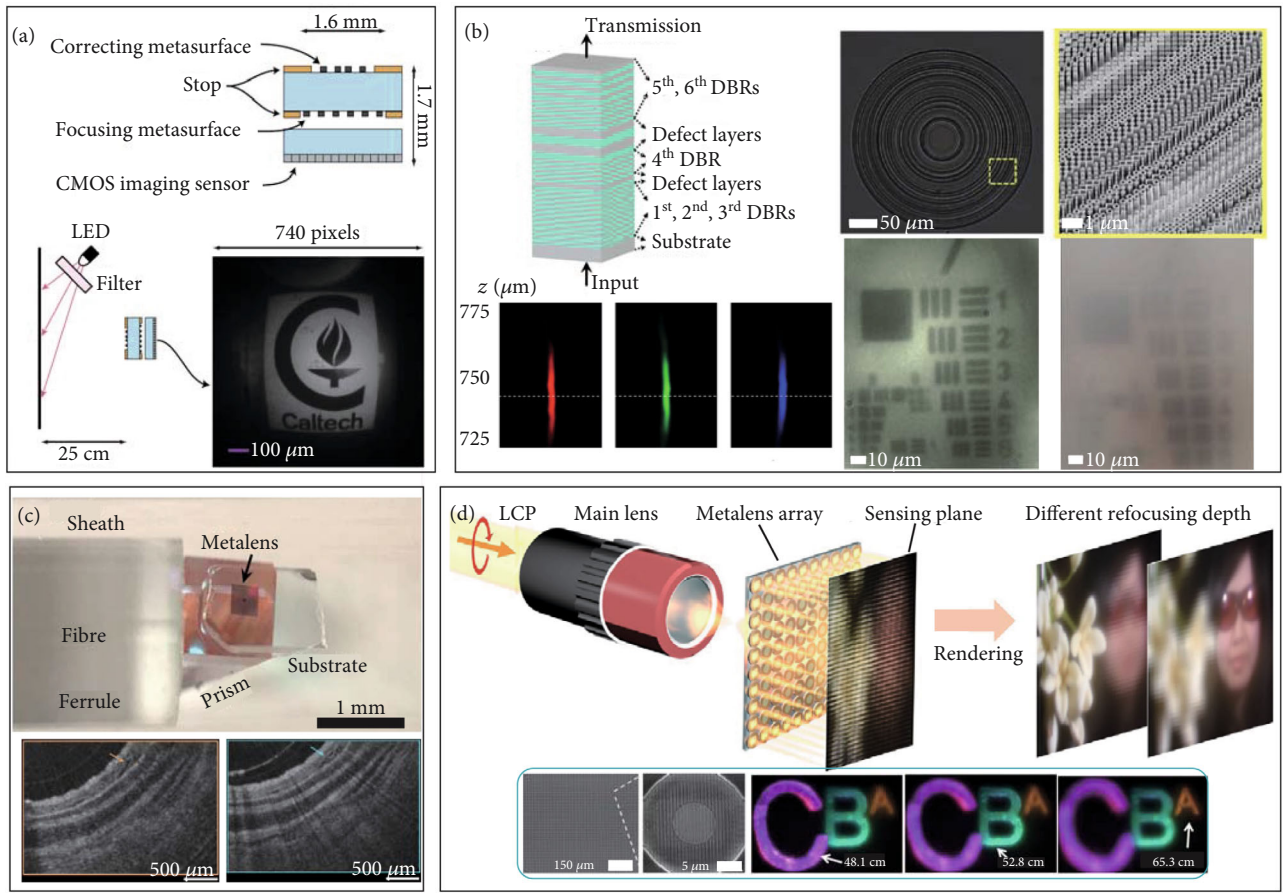


FIGURE 3: (a) Schematics of a metasurface-based miniaturized camera and the experimental setup for imaging quality characterization of the camera. Reproduced under the terms of the Creative Commons Attribution license (CC BY 4.0). https://creativecommons.org/licenses/by/4.0/ [84]. (b) A schematic of the sandwich configuration bandpass filter, SEM images of the fabricated metalens and its achromatic performance, and images captured under white light with (left) and without (right) the bandpass filter by the same metalens. Reproduced under the terms of the Creative Commons Attribution license (CC BY 4.0). https://creativecommons.org/licenses/by/4.0/ [93]. (c) Experimental assembly of the endoscope with metalens, images captured with a ball lens configuration (left) and a metalens configuration (right) endoscope. Reproduced with permission. Copyright 2018, published by Springer Nature [97]. (d) The light-field imaging system based on a metalens array, SEM images of the metalens array, and rendered images with different focusing distances. Reproduced with permission. Copyright 2019, published by Springer Nature [101].

Metalens also provides a pathway for the effective correction of existing imaging instruments. Figure 3(c) exhibits an endoscope in which a metalens replaced a conventional microlens to eliminate spherical aberrations and astigmatism, and the tailored chromatic dispersion was found to be helpful in achieving a larger imaging depth [97]. The fiber was responsible for delivery and subsequent collection of the light and sending the endoscope to hard-to-reach destinations. A higher image quality with the metalens compared to the conventional ball lens configuration was observed. Another metalens-based tomographic imaging instrument was proposed by redesigning the phase profile for spherical incident waves [98]. Exploiting metasurfaces to control other properties of light will enable more types of tomography and facilitate biochemical research and disease diagnosis.

Metasurface can arbitrarily design the focal spots, giving rise to novel functions, such as in-sensor computation. Three-dimensional depth sensing based on metalenses has been developed over the last few years [99–101]. For example, inspired by the light-field imaging theory, Lin et al. utilized an array containing $60 \times 60$ broadband achromatic metalenses to acquire a subimage array, and reconstruction of the scene was realized through arbitrarily rendering the images with different focusing distance based on these subimages [101], as shown in Figure 3(d). Inspired by the fact that jumping spiders decode depth information from a series of simultaneously obtained defocus images, Guo et al. utilized a metalens incorporating phase profiles of 2 off-axis lenses to split the incident light and the depth map was calculated by point spread function (PSF) analysis of 2 images with different defocus on the same sensing plan [102], as shown in Figure 4(a). Their methods require a low budget of computation; thus, a real-time operation is possible for compact systems.

The ultrathin, large NA metalenses are also a potential approach to address the challenges in miniaturized optical systems for augmented/virtual reality (AR/VR) [28, 103].

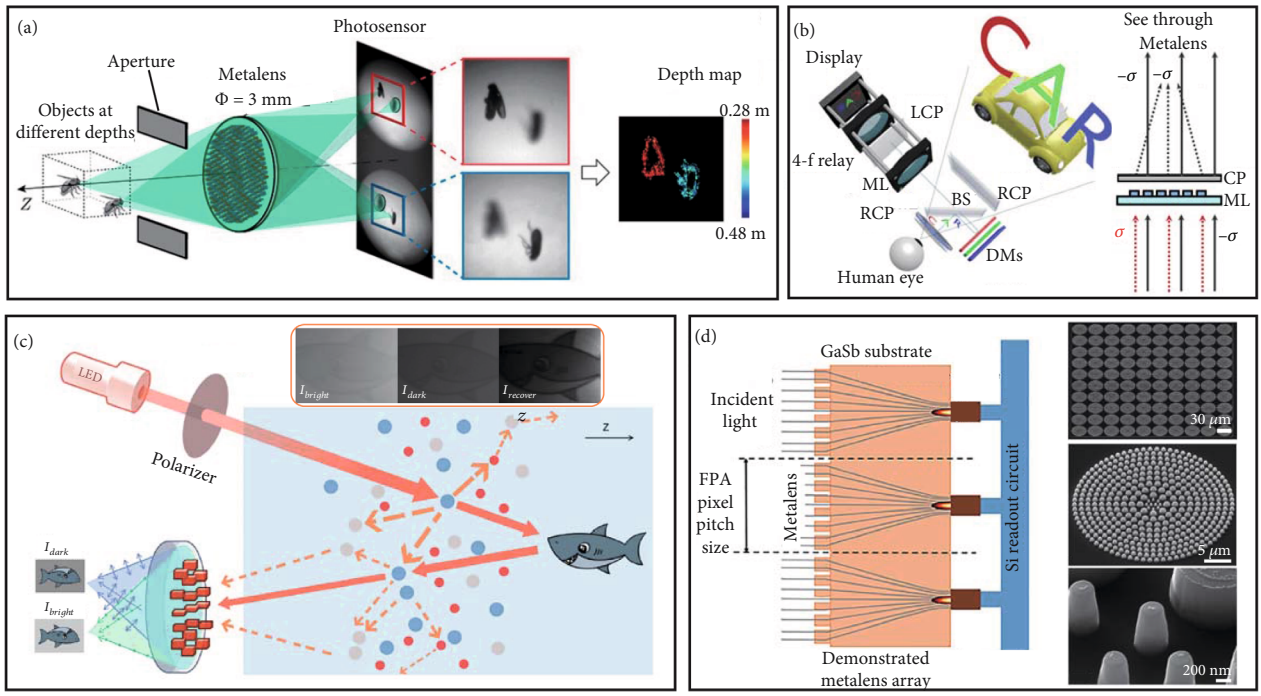


FIGURE 4: (a) A metalens-based depth sensor capturing two images of different defocus on the same image plane and corresponding depth map obtained by efficient calculations. Reproduced with permission. Copyright 2019, National Academy of Sciences [102]. (b) Illustration of the AR system based on a see-through metalens (ML). CP, LCP, RCP, BS, and DMs denote a circular polarizer, a left circular polarizer, a right circular polarizer, a beam splitter, and dichroic mirrors, respectively. Reproduced under the terms of the Creative Commons Attribution license (CC BY 4.0). https://creativecommons.org/licenses/by/4.0/ [28]. (c) Working principle of the underwater imaging apparatus, and the relatively bright image (left) and the relatively dark image (middle) captured of different polarization states. The recovered image (right) by polarization analysis. Reproduced with permission. Copyright 2021, Wiley-VCH [106]. (d) A schematic illustration of the architecture of the back-illuminated IR-FPA and SEM images of fabricated $10 \times 10$ metalens array. Reproduced with permission. Copyright 2018, AIP Publishing [107].

Lee et al. finished a prototype of AR glass system achieving a large field-of-view (90°) by incorporating a metalens with a relatively large diameter of 20 mm fabricated by nanoimprinting [28], as shown in Figure 4(b). For circularly polarized light, the metalens based on geometric phase design acts as transparent glass for copolarization transmission and a converging or diverging lens for cross-polarization transmission. This feature enabled the fusion of actual scenes and virtual objects, and the optimization was performed for copolarization mode to circumvent the distortion [28].

Capabilities of polarization-sensitive detection enable metalenses to acquire information unavailable from intensity or spectral analysis, which facilitates the implementation of polarization imaging using one optical component [104–106]. Recently, in order to circumvent the image blurring in underwater detection, Zhao et al. developed a metalens-based polarization imaging instrument assisted by the differences of polarization states between the light reflected from target objects and from unwanted background particles, and a proper estimation of extinction coefficients of the propagation medium begot accurate depth information (Figure 4(c)) [106].

Metalens arrays are applicable to implement high-performance IR focal plane arrays (IR-FPAs) with suppressed spatial cross talk and increased sensitivity operating at the room temperature [107, 108]. Zhang et al. designed an architecture of the back-illuminated IR-FPA with a solid-immersion metalens array fabricated through directly etching the GaSb substrate, the focal spots of which are located on pixels of the detector array embedded in the substrate [107], as shown in Figure 4(d). Implementation of the IR-FPA requires a large meta-atom array and monolithic integration with the detector array, and this will be enabled by the constant developing progress of the batch fabrication methods [29, 109]. The perfect absorbers enabled by infrared metasurfaces provide a new architecture of spectral selective infrared detectors [110]. Multifunctional metasurfaces consisting of structured metals and pyroelectric materials exploit the same structure for both optical enhancement and electrical readout. The metasurface-based detector provides a potential solution to implement compact, multicolor, and highly responsive infrared detectors for hyperspectral imaging.

In addition to the aforementioned research, metasurfaces have shown significant potential in light sources. Applications such as structural light projection [111], enhanced LED light extraction [112], radiation sources of X-ray [113], vacuum ultraviolet light [114], and IR light [115, 116] have been demonstrated. The versatile metasurfaces have enabled compact, multifunctional imaging systems.

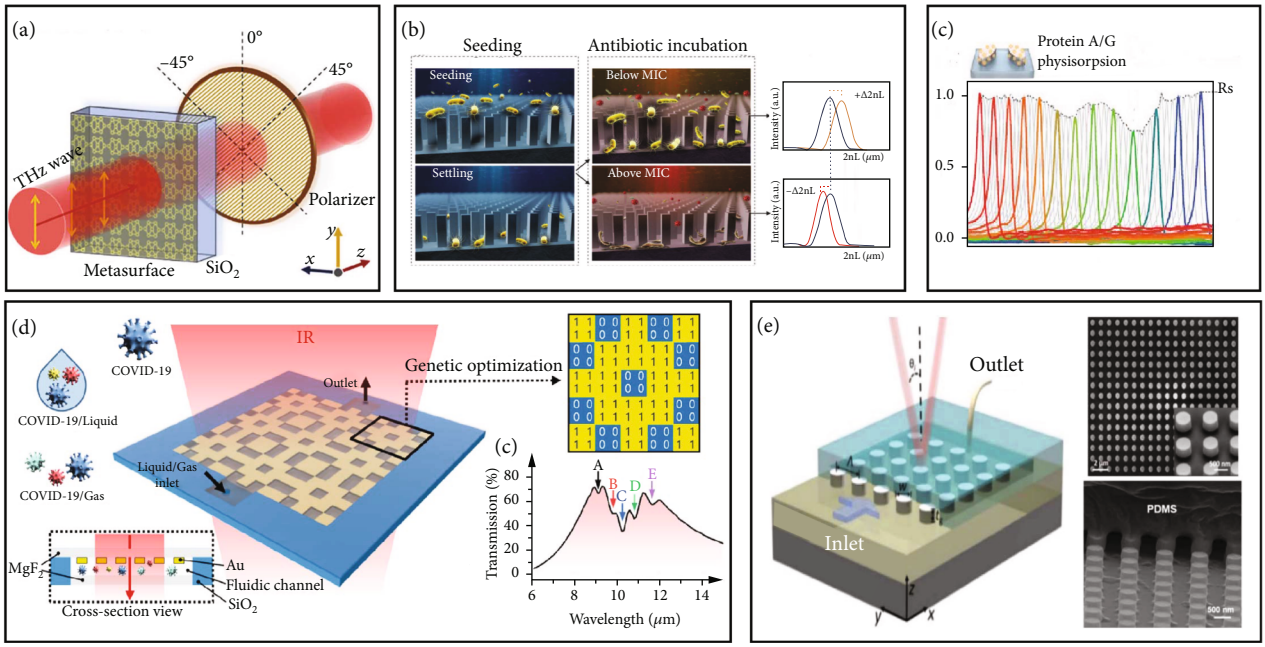


Figure 5: (a) Illustration of terahertz polarization detection and analysis metasurface for tumor cell antiproliferation. Reproduced under the terms of the Creative Commons Attribution license (CC BY 4.0). https://creativecommons.org/licenses/by/4.0/ [117]. (b) Conceptual image of different interactions between the bacteria and metasurface (left) and spectrum phase shift of the bacteria in different concentration of antibiotic incubation (right). Reproduced with permission. Copyright 2017, American Chemical Society [118]. (c) Conceptual image of the protein A/G coating on the metasurface (top), fingerprint figure of the protein A/G (bottom). Reproduced with permission. Copyright 2018, AAAS [21]. (d) Conceptual image of the virus detection and sorting metasurface (left) and spectrum of five intrinsic modes labeled in the COVID-19 (right). Reproduced with permission. Copyright 2021, American Chemical Society [120]. (e) Conceptual image of the optofluidic system based on metasurface technologies for cancer biomarker detection (left) and SEM images of the metasurface integrating in to the optofluidic (right). Reproduced with permission. Copyright 2018, Elsevier [121].

*3.2. Metasurfaces for Biological and Chemical Sensors.* Metasurfaces consisting of subwavelength and periodic structures enable high-performance biological and chemical detection. The resonant frequency of metasurfaces is controlled by the structures of the meta-atoms. High selectivity of metasurfaces based on the resonating nature and local field enhancement effects is achieved by matching the resonant mode of metasurfaces with the target. With the advantages of label-free, high-sensitivity, and good selectivity, some typical examples of metasurfaces are introduced herein to demonstrate the great potential to work as biochemical sensors.

*3.2.1. Metasurfaces in Biological Sensing.* Metasurface-based cancer cell detection method exhibits the capabilities of label-free, real-time, and in situ analysis of the cell proliferation to meet the requirements in modern cellular biological sensing. In order to increase the sensitivity, Liu et al. exploited the metasurface-based terahertz polarization sensing to analyze the antiproliferation of tumor cells with aspirin, as shown in Figure 5(a). The quality factor is 4~5 times higher with the terahertz (THz) polarization approach. The polarization ellipse of the output THz waves from the tumor cells (293T, B16, and HepG2) shows significant difference after aspirin treatment [117]. The polarization sensing technology amplifies the tumor cells' spectrum difference before and after the aspirin treating. The result demonstrates that the well-designed and portable THz metasurface provides a new route to the detection of antiproliferation in the tumor cell research area as well as other medical fields, potentially widely adopted in future clinical practices.

Mainstream antimicrobial susceptibility testing (AST) technologies of the current clinics have made a great improvement to the modern medical science. Combined with the metasurface, a new technology namely phase-shift reflectometric interference spectroscopic measurement (PRISM) was developed for AST [118], as shown in Figure 5(b). While the conventional AST technologies take around 20 hours to finish the entire process, the PRISM takes less than 5 h. The effect of antibiotic treatment can be identified by measuring the temporal responses of PRISM, determining the minimum inhibitory concentration (MIC). PRISM can find the most effective recipe of antibiotics for a special patient in a short time among a wide range of antibiotics. With the development of artificial intelligence, metasurface technologies may detect the mutation of the bacteria gene and the status of the porins on the bacteria membrane, thus providing more accurate information for doctors to find the suitable therapies.

Mid-IR spectrum, on the other hand, offers a nondestructive and label-free approach for biological molecule (proteins, lipids, and DNA) detection. However, due to the mismatch between mid-IR wavelengths and dimensions of molecules, the sensitivity of mid-IR is not enough to detect the nanometer-scale samples (biological membranes). In order to improve the sensitivity and tell the unique

fingerprint of the nanometer-scale biological molecules (protein, lipids, and DNA), a new method based on the mid-IR metasurface is proposed. When the resonance spectrum of the metasurface is overlapped with the absorption fingerprints of the molecules, either the frequency or the strength of the resonance will be changed. This concept is called surface-enhanced IR absorption (SEIRA) [21], as shown in Figure 5(c). Distinct biological molecule absorption fingerprint is originating from the amid I and amid II vibrational bands located near 1660 $cm^{-1}$ and 1550 $cm^{-1}$, respectively. With the special structural design, the mid-IR metasurface has the extremely high $Q$ ($Q > 200$) absorption spectrum peaks between 1350 $cm^{-1}$ and 1750 $cm^{-1}$ with a gap 60 $cm^{-1}$, which is much narrower than the spectral feature size of the individual amide I and II absorption band. Therefore, the SEIRA metasurface can easily distinct the different biological molecules and quantify the molecules concentrations with artificial intelligence (AI), facilitating the improvement in biosensing. The ubiquitous SEIRA is foreseeable by decreasing the cost in material and fabrication processes of the nanostructures [119]. Aluminum plasmonic disks were fabricated using colloidal mask processes to form infrared metamaterial perfect absorbers. The absorbers were functionalized using phosphonic acid and enhance the absorbance response of bovine serum albumin by at least 8 times with the surface plasmonic enhancement effect. These works pave a way to achieve highly sensitive biomolecule detection using SEIRA.

In addition to bacteria and biomolecule detection, metasurface can provide an efficient tool for virus screening and detection. For example, in order to realize fast diagnosis of COVID-19, IR metasurface is developed as an alternative approach to achieve high-efficiency patient screening. COVID-19 is induced by a new coronavirus consisting of single-stranded positive-sense RNA genome and four structural proteins (spike surface glycoprotein (S), small envelope protein (E), matrix protein (M), and nucleocapsid protein (N)) [120]. Each of them has different resonance frequencies. The normal and mutation viruses are capable to be distinguished with these 5 absorption peaks by artificial intelligence IR metasurface. This metasurface biosensor with an ultrahigh sensitivity (1.66%/nm) has a wide detection range within the diversity detection environment (gas/liquid), as shown in Figure 5(d). It provides a pathway towards the ultrarapid, label-free, multifunctional, and unique IR fingerprint detection of the COVID-19. The ability of the mutation virus detection can make great efforts to address the current global pandemic.

Besides standalone metasurface membranes for biological spectrum detection, metasurfaces can be integrated into lab-on-a-chip devices to achieve advanced functions. For example, classical microfluidic devices based on the binding assays which require fluorescent or enzymatic tags have done the great contributions to biological detection [121]. Metasurface integrated into the microfluidic devices called "optofluidic" is the label-free assays which eliminate the need for time-consuming labeling process and can monitor binding kinetics in real time. In order to realize the early diagnosis of cancer patients, a novel lateral flow-through biosensor consisting of a metasurface with a two-dimensional (2D) periodic array of silicon nanoposts (SNPs) is reported to detect cancer biomarker, as shown in Figure 5(e). With the incident angle 1°, the absorption peaks of the metasurface will get the highest $Q$ value [121]. By the spectral analysis, the antigen and antibody binding process can be observed as the spectral shifts. Overall, the optofluidic devices offer a new insight of the biomolecule detection technology and give a new direction of the metasurfaces integrated devices. Combined with the deep learning technologies, this system may have the great potential in diagnosis of a wide range of diseases.

*3.2.2. Metasurfaces in Chemical Sensing.* Gaseous target detection and quantitative remote sensing attract massive efforts in metasurface-assisted spectral analysis technologies. In order to achieve highly sensitive gas detection, metasurfaces integrated with metal organic frameworks (MOFs) are introduced. It provides both excellent absorption selectivity and high gas affinity [122]. With the design of the metasurface, the absorption peaks are adjusted to the wavelength range between 4.25 $\mu$m and 7.66 $\mu$m to match the vibration modes of the $CO_2$ and $CH_4$, as shown in Figure 6(a) [122]. After modifying the surface with MOFs, the absorption peak value increases from 0.022 to 0.221. The MOF-SEIRA platform achieves simultaneous on-chip sensing of $CO_2$ and $CH_4$ with the fast response time (<60 s), high accuracy (CO2: 1.1%, CH4: 0.4%), small footprint ($100 \times 100$ $\mu m^2$), and excellent linearity in a wide dynamic range ($0 - 2.5 \times 10^4$ ppm).

To meet the demands of rapid, low cost, and portable deployment, a metasurface based on the multiwalled carbon nanotubes is developed to detect chemical residues, such as pesticides. The limited performance of the traditional metasurface with metallic meta-atoms is mainly due to inherent losses in metals. Alternatively, carbon nanotubes with the outstanding electrical and optical properties offer the new opportunities for applications in THz science and technology, as shown in Figure 6(b). Different concentrations of pesticides (2,4-dichlorophenoxyacetic and chlorpyrifos solutions) can be detected by this new platform with lowest detection mass of 10 ng and the sensitivities of $1.38 \times 10^{-2}$/ppm and $2.0 \times 10^{-3}$/ppm, respectively [123]. Good linear relationship between transmission amplitude and pesticide concentration, acceptable reliability, and stability can be achieved in this multiwalled carbon nanotube metasurface-based chemical sensing platform.

In addition to pesticides, metasurface may also be employed in quantitative sensing of specific drugs for healthcare applications. In order to monitor the harmful effects of the drug abuse, a rapid, noninvasive, accurate detecting method is highly desired. To meet these demands, the metasurface is a candidate due to the improved signal to noise ratio in the spectroscopy. A new metasurface based on the hybrid Au/Ag hybrid nanoparticles is proposed to work as a surface-enhanced Raman spectrometry (SERS) substrate, as shown in Figure 6(c). Combining with the Raman spectroscopy, the obvious Raman peaks of cocaine at 1001 $cm^{-1}$, 1027 $cm^{-1}$, 1275 $cm^{-1}$, and 1598 $cm^{-1}$ can be

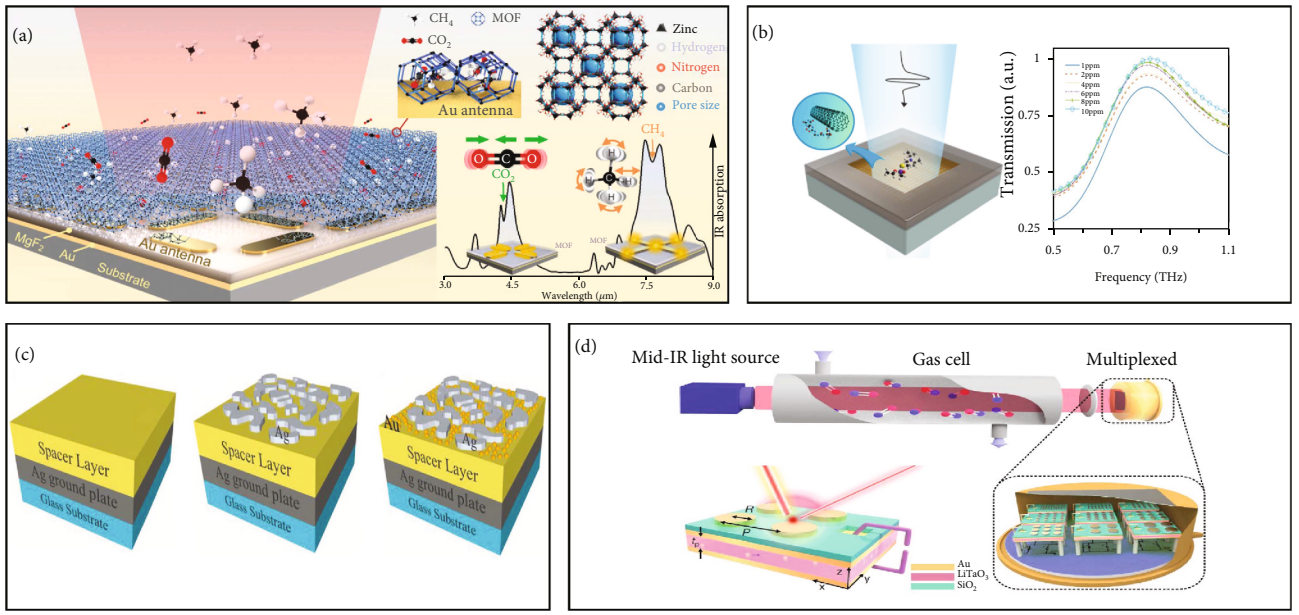


FIGURE 6: (a) Schematic of gas detection and analysis metasurface with MOFs modified (left) and intrinsic vibration spectrum of the different gases (right). Reproduced with permission. Copyright 2020, Wiley-VCH [122]. (b) Illustration of carbon nanotubes metasurface platform for pesticides residue detecting (left) and transmission spectrum of the different concentrations of the pesticide (right). Reproduced with permission. Copyright 2020, American Chemical Society [123]. (c) Conceptual image of metasurface platform based on the hybrid of Au/Ag nanoparticles for drug (cocaine) quantitative analysis. Reproduced with permission. Copyright 2018, Wiley-VCH [124]. (d) Illustration of gas sensing system "photonic nose" based on mid-IR metasurface for different gases sensing. Reproduced under the terms of the Creative Commons Attribution license (CC BY 4.0). https://creativecommons.org/licenses/by/4.0/ [125].

observed with the concentration as low as 10 $\mu$g/mL. Considering the metasurface area 20 mm$^2$, the average of the detection limit is 5 ng/mm which is outperforming previous results [124]. Therefore, metasurface is a potential solution to develop highly sensitive, low cost sensors for therapeutic drug monitoring.

Metasurfaces can be integrated in the optoelectronic detectors to form a compact system for chemical detection. In order to detect the target gas, the IR detector has to pair with a band pass filter making the sensor bulky and expensive. A new gas sensing platform is proposed by integrating the pixeled metasurface absorber into the detector to solve this shortcoming, as shown in Figure 6(d). By modifying the geometry of metallic plasmonic resonators, the central wavelength of each pixeled cell can be independently fitted the characteristic absorption bands of different target gases. With the metasurface design, the platform can sense different gases, including $H_2S$, $CH_4$, $CO_2$, CO, NO, $CH_2O$, $NO_2$, and $SO_2$ with the detection limits of 489, 63, 2, 11, 17, 27, 54, and 104 ppm, respectively [125]. The concentrations of gases in mixtures can be detected by multiple narrowband detectors. In the future, with the development of the MEMS technologies, integrated multiplexed gas sensors with miniaturized dimension can be achieved.

*3.3. Metasurfaces for Multifunctional Optoelectromechanical Systems.* Metasurfaces, composed of subwavelength meta-atoms, have demonstrated unprecedented capabilities for manipulating EM waves from the microwave to optical regimes [126–128]. However, most of early generation metasurfaces were static, and their EM responses were immutable due to the fixed configurations. Tunable and reconfigurable metasurfaces are able to achieve dynamic manipulation of EM waves towards multifunctional optoelectromechanical systems. Since the EM responses are tuned in the subwavelength scale, the modulation efficiency of the device is high, fulfilling the requirements of intelligent and integrated devices and instruments, such as advanced wireless communications [129, 130], LiDAR [19], and dynamic holography [131, 132]. In the microwave range, active electronic devices (varactors, diodes, and semiconductor switches) have been integrated with the meta-atoms to control the EM waves dynamically [133, 134]. Combined with the digital controllers, the programmable metasurface systems are realized [135]. When the working wavelength of reconfigurable metasurfaces moves from the microwave to the THz, IR, or even the visible regime, additional tuning mechanisms based on various materials, including liquid crystals [136, 137], 2D materials [138–140], phase change materials (PCMs) [141, 142], and epsilon-near-zero (ENZ) thin films [143, 144], have been explored to dynamically control EM responses.

The demonstration of an on-chip electrical switching metasurface platform based on the PCM, such as $Ge_2Sb_2Se_4Te$ (GSST), was developed to enable binary switching and beam steering at the 1550 nm wavelength, as shown in Figure 7(a) [141]. In this design, a large-scale GSST Huygens' metasurface was fabricated on an optimized metallic heater (reflector), and the device was wire bonded and mounted onto a PCB. The phase (amorphous/crystalline) of the PCM was changed by electrical pulsing to tune the

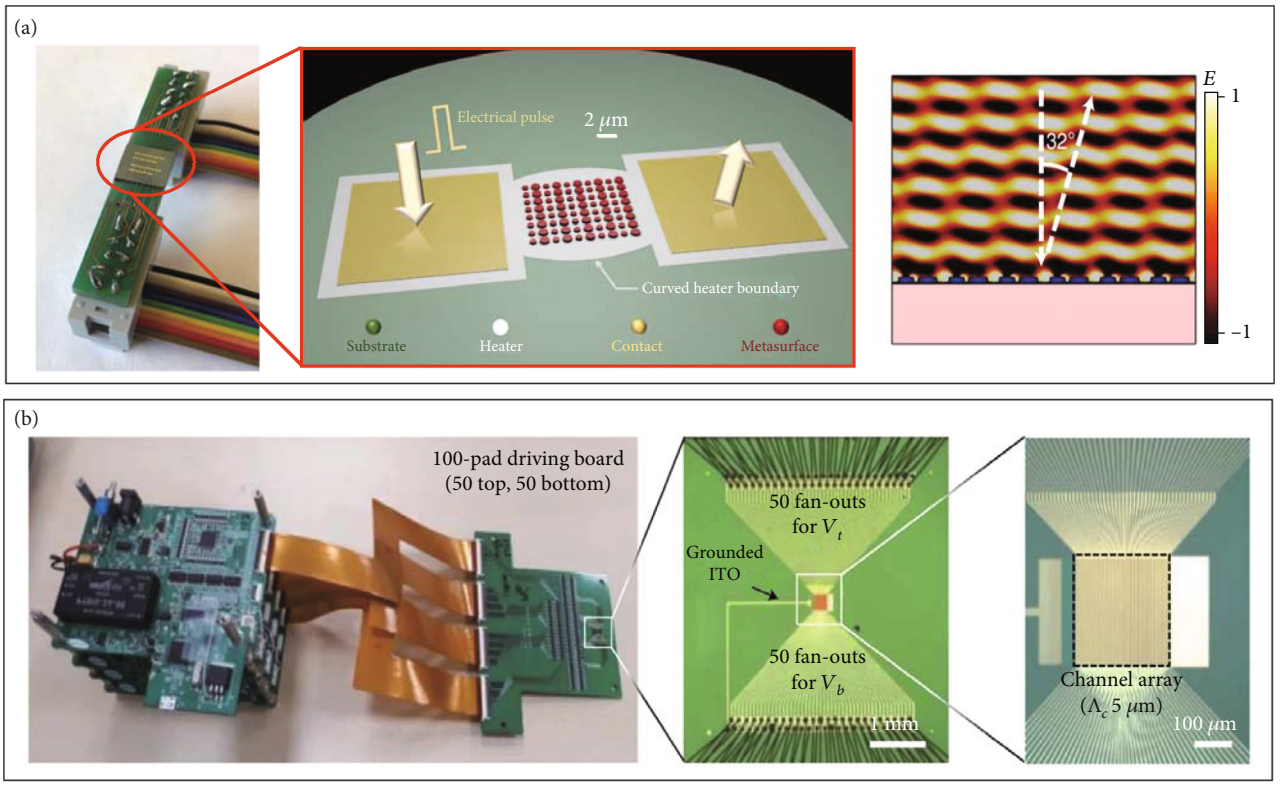


FIGURE 7: Electrical reconfigurable metasurfaces based on (a) phase change materials (PCM) [141] and (b) epsilon-near-zero (ENZ) thin films [143]. (a) Reproduced with permission. Copyright 2021, published by Springer Nature. (b) Reproduced with permission. Copyright 2021, published by Springer Nature.

amplitude and phase responses. This electrically reconfigurable metasurface is capable of deflecting beam with an angle of 32°. In addition, ENZ thin films, such as doped semiconductors and transparent conducting oxide (TCO) materials, have also been employed in metasurfaces to realize advanced optical systems. As shown in Figure 7(b), an array of Au plasmonic nanoresonators (top layer) and an Al mirror (bottom layer) were separated by an indium tin oxide (ITO) layer (middle layer) [143]. The charge depletion layers were formed at the upper and lower interfaces between the ITO layer and the insulting oxide layers by applying two appropriate gate voltages to shift the phase responses in a wide range. The integrated spatial light modulator consisted of an active metasurface, including 550 individually addressable nanoresonators, and the driving electronics have been applied in constructing LiDAR in the NIR regime.

High-resolution spatial light modulators are a class of optical devices that create arbitrary light patterns. Metasurfaces enable efficient spatial light modulation at long-wave infrared, terahertz, and microwave regimes. Spatial light modulators based on tunable metasurfaces with semiconductors [145] and liquid crystals [146] have given rise to single pixel and computational imaging systems. More comprehensive overview of metasurface-based spatial light modulator may be found in the latest review [147].

Besides, MEMS-based tunable/reconfigurable metasurfaces are capable of manipulating the near-field interactions between meta-atoms significantly by the mechanical deformation to achieve tunable response [148, 149]. Massive efforts have been made to develop MEMS-based reconfigurable metasurfaces due to their large tunability and high-power handling capabilities [150].

*3.3.1. Modulation of Amplitude and Polarization.* The homogenously reconfigured metasurfaces can efficiently modulate the amplitude [151–153] and polarization [33, 154, 155] of EM waves. For example, arrays of split ring resonators were fabricated on bimaterial cantilevers to form the first integration scheme of a mechanically reconfigurable metasurface [151]. In this design, the bimaterial cantilevers underwent mechanical deformation by a thermal stimulus, and the EM responses were tunable. Many mechanically reconfigurable metasurfaces were then developed from the terahertz to optical regime. To increase the diversity of functions, a MEMS-based reconfigurable metasurface with multiple-input–output (MIO) states was demonstrated, as shown in Figure 8(a) [129, 130]. In this design, logic operations (XOR, XNOR, and NAND) were exhibited with two independently controlled electrical inputs and an optical output at terahertz frequencies. The device served as an important tool for the cryptographically secured terahertz wireless communication. Recently, a novel reconfigurable metasurface platform with combined tuning mechanisms has been demonstrated to be capable of realizing the efficiently multidomain control of terahertz waves [156]. As shown in Figure 8(b), a microcantilever array was fabricated

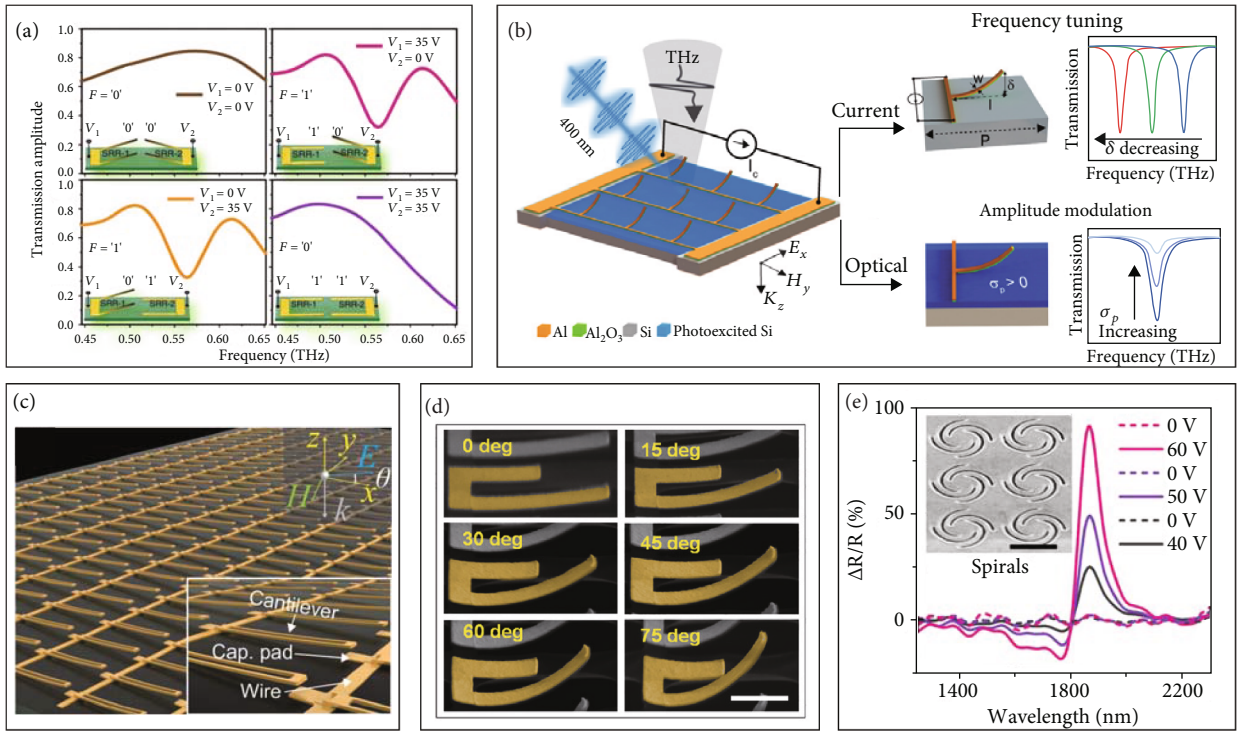


FIGURE 8: MEMS-based reconfigurable metasurfaces for amplitude and polarization modulation. (a) MEMS metasurfaces for logic operations at terahertz frequencies. Reproduced under the terms of the Creative Commons Attribution license (CC BY 4.0). https://creativecommons.org/licenses/by/4.0/ [130]. (b) Independent manipulation of amplitude and frequency responses by reconfigurable microcantilever at terahertz frequency. Reproduced with permission. Copyright 2021, Wiley-VCH [156]. (c) MEMS-tunable metasurface transmission waveplate at terahertz frequencies. Reproduced under the terms of the Creative Commons Attribution license (CC BY 4.0). https://creativecommons.org/licenses/by/4.0/ [33]. (d) Chiral metasurface based on 3D bended split ring resonators. Reproduced with permission. Copyright 2021, Wiley-VCH [155]. (e) Electromechanically reconfigurable nanokirigami at optical wavelengths. Reproduced under the terms of the Creative Commons Attribution license (CC BY 4.0). https://creativecommons.org/licenses/by/4.0/ [169]. The unit cell of the metamaterial: (a) $P_x = 110\ \mu$m and $P_y = 75\ \mu$m, (b) 120 $\mu$m, and (e) 2.25 $\mu$m.

on an ion-irradiated silicon substrate to achieve the advanced spatiotemporal modulator. In this design, the MEMS tuning and femtosecond laser pulses provided large spectral tunability and ultrafast amplitude modulation, respectively.

In addition to tuning amplitude, the polarization of EM waves is also desirable to be modulated dynamically. To obtain ultrathin tunable optical components, a birefringent reconfigurable metasurface was proposed to replace traditional polarization modulators based on birefringent materials. In this design, an Au nanograting was fabricated on the out-of-plane electrostatic MEMS actuator [157]. The retardation was modulated from 21.5° to 46.8° at a wavelength of 633 nm with an actuation voltage of 0–200 V.

The anisotropic behavior for different polarization angles is introduced by the asymmetrically structured unit cells [158, 159]. MEMS actuators not only break the symmetry of symmetrical meta-atoms [154] but also generate different EM responses in asymmetrical meta-atoms [36, 160]. With a microcantilever array design, the anisotropic reconfigurable metasurface was able to change the polarization of transmitted EM waves from circular to linear at 0.81 THz by a voltage of 40 V, as shown in Figure 8(c) [33]. In the polarization tunable metasurface, the single-layer microcantilevers were fabricated on a silicon substrate, which was coated with an insulating silicon nitride thin film using surface micromachining. This CMOS-compatible reconfigurable terahertz metasurface is able to be applied in material characterization and enhanced imaging. Furthermore, chiral metasurfaces are important for numerous applications such as optical circular polarizers, chiral light imaging [161], and quantum computing [162]. As depicted in Figure 8(d), an array of asymmetric bended split ring resonators (SRRs) exhibited giant chiroptical responses at 5.2 $\mu$m due to the symmetric breaking along $z$-axis [155]. The bending angle of the 3D SRR was tuned by the tensile stress resulted from focused ion beam (FIB). The measured CD was -0.29 for the forward incidence and 0.71 for the backward incidence at a bending angle of 60°.

Different from the standard MEMS processes, nanoorigami/kirigami provides an efficient microfabrication/nanofabrication for transforming planar sheets into 3D structures [163, 164]. To date, origami/kirigami-based metasurfaces have been applied in modulating amplitude [165, 166] and chirality responses [167, 168]. In an electromechanically reconfigurable optical nanokirigami shown in Figure 8(e), the modulation contrast achieved 88% and 494% at 953 nm and 1734 nm by controlling the applied

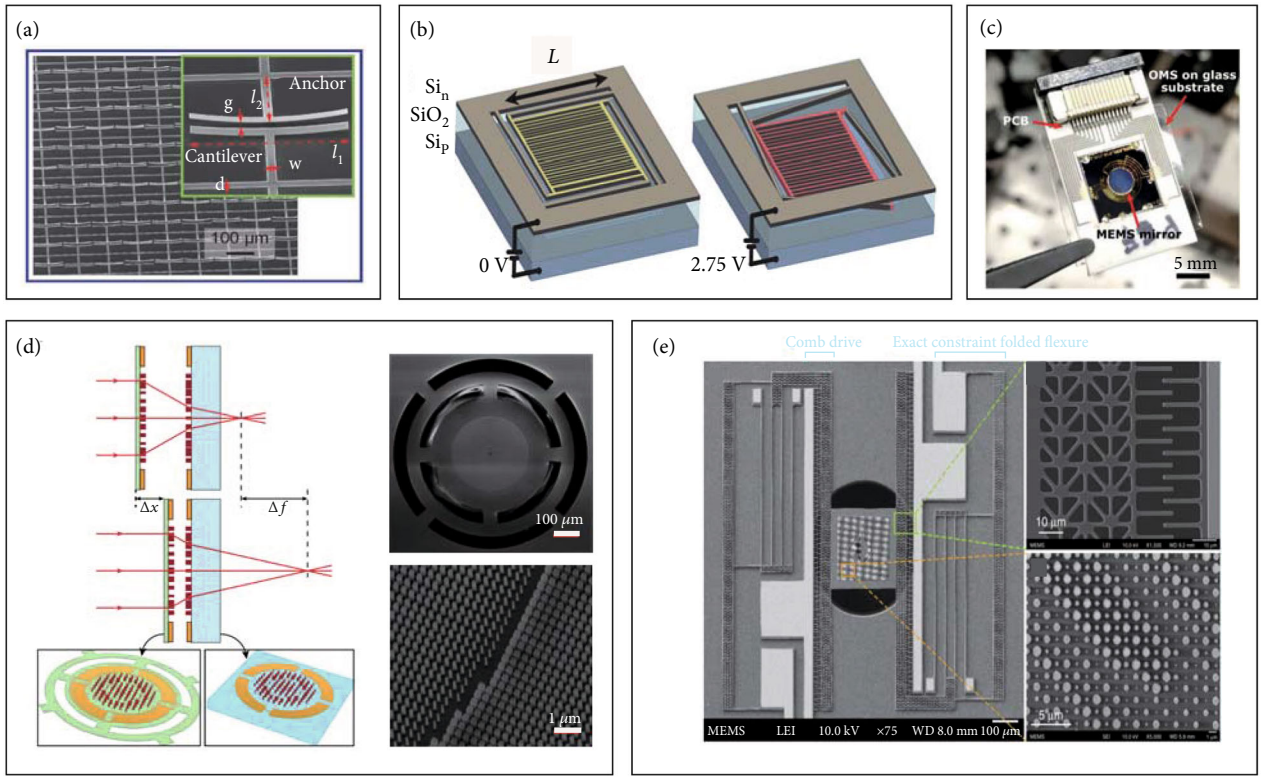


FIGURE 9: MEMS-based reconfigurable metasurfaces for wavefront manipulation. (a) Active multifunctional MEMS metasurface devices used in wavefront deflection and holograms. Reproduced with permission. Copyright 2016, Wiley-VCH [36]. (b) Dynamic beam shaping with silicon metasurfaces. Reproduced with permission. Copyright 2019, AAAS [171]. (c) Dynamic piezoelectric MEMS-based optical metasurfaces. Reproduced under the terms of the Creative Commons Attribution-NonCommercial license (CC BY-NC 4.0). https://creativecommons.org/licenses/by-nc/4.0/ [172]. (d) A MEMS-tunable dielectric metasurface lens. Reproduced under the terms of the Creative Commons Attribution license (CC BY 4.0). https://creativecommons.org/licenses/by/4.0/ [173]. (e) MEMS-actuated metasurface Alvarez lens. Reproduced under the terms of the Creative Commons Attribution license (CC BY 4.0). https://creativecommons.org/licenses/by/4.0/ [174]. The periodicity of the silicon nanowire array in (b) is 300 nm.

voltage, respectively [169]. The dynamic modulation frequency was measured up to 200 kHz, which exhibited a high modulation speed in electromechanical optical reconfigurations. Recently, eight electromechanical nanokirigami structures with different azimuth angles were proposed to cover the $2\pi$ phase difference under a single-voltage control at visible wavelengths [170].

*3.3.2. Dynamic Wavefront Manipulation.* To manipulate wavefront dynamically, the early scheme of MEMS-based reconfigurable metasurface with the local control strategy was presented at terahertz frequencies [36]. As shown in Figure 9(a), the suspension angle of each bimorph cantilever was precisely controlled by the applied voltage. In this device, beam steering and holographic display was realized through 1D and 2D encoding of unit cells, respectively. However, the global control approach was commonly used due to the feature size of the meta-atoms operated in the IR and visible range [171–174]. As shown in Figure 9(b), the dynamic wavefront shaping was achieved by silicon antenna arrays, which were fabricated by the standard silicon-on-insulator (SOI) technology [171]. In this scheme, the width of the high-index Si nanobeams (100 nm thick) increased from 80 nm to 160 nm. The gap between the Mie resonator-based metasurfaces and the Si substrate was changed with the different actuation voltage (<4 V), and the deflection angle was changed from 2° to 12° at a wavelength of 600 nm. Gap surface plasmon- (GSP-) based gradient metasurfaces are possible solutions for controlling light at the nanoscale [175, 176]. As depicted in Figure 9(c), an optical metasurface (OMS) has been combined with a thin-film piezoelectric MEMS mirror to form the GSP-based MEMS-OMS platform [172]. The phase and amplitude of the reflected light were well modulated by varying the small air gap between the OMS and the MEMS mirror. By adjusting the applied voltage within the range of 3.75 V, dynamic polarization-independent beam steering and reflective 2D focusing have been experimentally demonstrated. The beam steering efficiency reached about 50% at an operating wavelength of 800 nm, and the rise/fall times of the MEMS-based device were less than 0.4 ms.

Tunable metalenses are an important component for intelligent optical systems [173, 177]. In the early concept of dynamic metalens based on MEMS technology, a 10 $\mu$m thick metasurface-based flat lens was attached onto the processed MEMS actuator [177]. However, the monolithic integration of MEMS and metasurfaces was not realized in this design, and it required delicate operation to combine the

two components. Subsequently, a focal-tunable metalens with two layers of all-dielectric metasurfaces generated more than 60 diopters changes at 915 nm wavelength when one metasurface moves 1 $\mu$m, as shown in Figure 9(d) [173]. In this design, the stationary and moving metasurfaces were patterned on a glass substrate and a silicon nitride membrane, respectively. The focal point was modified by controlling the distance between the two Si metasurfaces using electrostatic forces. In addition, the optical intensity is able to be modulated by Alvarez lenses, which consist of paired optical elements with complementary cubic surface profiles [178, 179]. According to the Alvarez principle, the focal length is varied when there is a relative lateral displacement between the two identical elements. Currently, an ultrathin Alvarez lens based on metasurfaces was presented to replace the conventional bulky optical element that needs the complicated fabrication [180, 181]. As illustrated in Figure 9(e), a silicon nitride metasurface-based Alvarez lens yielded a total in-plane displacement of 6.3 $\mu$m with an actuation voltage of 20 V, and a tuning range of 68 $\mu$m in focus was produced at 1550 nm wavelength [174].

The MEMS-based tunable metasurfaces are an alternative approach to conventional optical MEMS devices, such as digital mirror devices (DMDs), in some applications. DMDs are well known for the capability of modulating the amplitude of light using micro mirror arrays. They are widely employed in displays, laser 3D printing, adaptive optics, and optical imaging, among others [182]. The dimension of each MEMS mirror in DMDs is usually larger than $10\mu\text{m} \times 10\mu\text{m}$, and the band of the dynamic tuning is ~1 kHz, enabling fast modulation and wide-angle optical beam manipulation. The MEMS-based tunable metasurfaces may not only modulate the amplitude but also provide additional functions, such as modulating the phase, wavefront, and polarization. Moreover, the tunable meta-atoms may modulate light at the subwavelength scale, giving rise to larger tuning range of the optical response with microscale physical displacement [171]. However, metasurfaces exhibit high dispersion and limited spectral bandwidth, while DMDs can efficiently modulate light over a wide spectrum. Therefore, the MEMS-based tunable metasurfaces may be an alternative approach and provide additional tunability to DMD for narrow band applications.

## 4. Conclusion

Metasurfaces provide a platform to manipulate EM waves in classical optics, and the interests in exploiting novel functions based on flat, metasurface optics in the quantum optics are increasing dramatically. The quantum states of photons include, but not limited to, the polarization, momentum, and orbital angular momentum, which might be controlled by metasurfaces as discussed above. For instance, metalens array fabricated on the nonlinear crystal, such as barium borate (BBO), is capable of generating the spontaneous parametric down-conversion photon source to demonstrate the multiphoton quantum entanglement for on-chip, integrated quantum devices. The metasurfaces, or meta-atoms, can be modulated in space and time, giving rise to dynamically tunable quantum correlation for nonreciprocal quantum routers and isolators. In addition to quantum phenomena, photonic topological insulators, parity-time symmetry, and exceptional points are enabled by coupled metasurfaces, which hold the promise to control the propagation of photons and EM waves in desired ways and bring novel functions. It is difficult to cover every aspect of metasurfaces in a review article. The development of metasurface theory and physics may be found in other review articles, such as [5, 8, 9, 60], and the myriad applications of metasurfaces may be found elsewhere [47, 65, 74]. As complementary to the published review articles, our review provides insights of metasurface applications in advanced devices and instrument.

In summary, metasurfaces can manipulate the propagating wavefront and near-field confinement by engineering meta-atoms. The extraordinary optical response may improve the performance of microsystems for imaging and sensing applications. In turn, the integration of MEMS with metasurfaces enables dynamically tunable optical responses, paving the way towards intelligent microsystems with capability of arbitrary control over the EM waves.

## Conflicts of Interest

The authors declare no competing interests.

## Authors' Contributions

X. Z., Z. S., L. Z., Z. W., and R. Y. wrote the manuscript. All the authors discussed the results and commented on the manuscript.

## Acknowledgments

This work is supported by the National Natural Science Foundation of China (Grant No. U21A6003), the Beijing Natural Science Foundation (Grant No. 422068), the Beijing Nova Program (Grant No. Z211100002121075), and the Young Elite Scientist Sponsorship Program by CAST (Grant No. YESS20210023). X. Z. acknowledges the startup funding from Tsinghua University. We would like to thank Dr. Kaisi Xu and Dr. Xiangyu Li for the helpful discussion.

## References

[1] S. Zhang, W. Fan, N. C. Panoiu, K. J. Malloy, R. M. Osgood, and S. R. J. Brueck, "Experimental demonstration of near-infrared negative-index metamaterials," *Physical Review Letters*, vol. 95, no. 13, article 137404, 2005.

[2] J. B. Pendry, A. J. Holden, D. J. Robbins, and W. J. Stewart, "Magnetism from conductors and enhanced nonlinear phenomena," *IEEE Transactions on Microwave Theory and Techniques*, vol. 47, no. 11, pp. 2075–2084, 1999.

[3] J. K. Gansel, M. Thiel, M. S. Rill et al., "Gold helix photonic metamaterial as broadband circular polarizer," *Science*, vol. 325, no. 5947, pp. 1513–1515, 2009.

[4] D. Schurig, J. J. Mock, B. J. Justice et al., "Metamaterial electromagnetic cloak at microwave frequencies," *Science*, vol. 314, no. 5801, pp. 977–980, 2006.

[5] M. Kadic, G. W. Milton, and M. Wegener, "3D metamaterials," *Nature Reviews Physics*, vol. 1, pp. 198–210, 2019.

[6] N. Yu, P. Genevet, M. A. Kats et al., "Light propagation with phase discontinuities: generalized laws of reflection and refraction," *Science*, vol. 334, no. 6054, pp. 333–337, 2011.

[7] X. Ni, N. K. Emani, A. V. Kildishev, A. Boltasseva, and V. M. Shalaev, "Broadband light bending with plasmonic nanoantennas," *Science*, vol. 335, no. 6067, p. 427, 2012.

[8] H.-T. Chen, A. J. Taylor, and N. Yu, "A review of metasurfaces: physics and applications," *Reports on Progress in Physics*, vol. 79, no. 7, article 076401, 2016.

[9] N. Yu and F. Capasso, "Flat optics with designer metasurfaces," *Nature Materials*, vol. 13, no. 2, pp. 139–150, 2014.

[10] M. Khorasaninejad, W. T. Chen, R. C. Devlin, J. Oh, A. Y. Zhu, and F. Capasso, "Metalenses at visible wavelengths: diffraction-limited focusing and subwavelength resolution imaging," *Science*, vol. 352, no. 6290, pp. 1190–1194, 2016.

[11] N. K. Grady, J. E. Heyes, D. R. Chowdhury et al., "Terahertz metamaterials for linear polarization conversion and anomalous refraction," *Science*, vol. 340, no. 6138, pp. 1304–1307, 2013.

[12] F. Aieta, P. Genevet, N. Yu, M. A. Kats, Z. Gaburro, and F. Capasso, "Out-of-plane reflection and refraction of light by anisotropic optical antenna metasurfaces with phase discontinuities," *Nano Letters*, vol. 12, no. 3, pp. 1702–1706, 2012.

[13] J. He, X. Wang, D. Hu et al., "Generation and evolution of the terahertz vortex beam," *Optics Express*, vol. 21, no. 17, pp. 20230–20239, 2013.

[14] M. Liu, H. Y. Hwang, H. Tao et al., "Terahertz-field-induced insulator-to-metal transition in vanadium dioxide metamaterial," *Nature*, vol. 487, no. 7407, pp. 345–348, 2012.

[15] J.-Y. Ou, E. Plum, J. Zhang, and N. I. Zheludev, "Giant nonlinearity of an optically reconfigurable plasmonic metamaterial," *Advanced Materials*, vol. 28, pp. 729–733, 2015.

[16] N. A. Estep, D. L. Sounas, J. Soric, and A. Alù, "Magnetic-free non-reciprocity and isolation based on parametrically modulated coupled-resonator loops," *Nature Physics*, vol. 10, no. 12, pp. 923–927, 2014.

[17] L. Zhang, X. Q. Chen, R. W. Shao et al., "Breaking reciprocity with space-time-coding digital metasurfaces," *Advanced Materials*, vol. 31, no. 41, article 1904069, 2019.

[18] L. Feng, Y.-L. Xu, W. S. Fegadolli et al., "Experimental demonstration of a unidirectional reflectionless parity-time metamaterial at optical frequencies," *Nature Materials*, vol. 12, pp. 108–113, 2012.

[19] I. Kim, R. J. Martins, J. Jang et al., "Nanophotonics for light detection and ranging technology," *Nature Nanotechnology*, vol. 16, no. 5, pp. 508–524, 2021.

[20] K. Fan, J. Y. Suen, X. Liu, and W. J. Padilla, "All-dielectric metasurface absorbers for uncooled terahertz imaging," *Optica*, vol. 4, no. 6, pp. 601–604, 2017.

[21] A. Tittl, A. Leitis, M. Liu et al., "Imaging-based molecular barcoding with pixelated dielectric metasurfaces," *Science*, vol. 360, no. 6393, pp. 1105–1109, 2018.

[22] X. G. Zhang, W. X. Jiang, H. L. Jiang et al., "An optically driven digital metasurface for programming electromagnetic functions," *Nature Electronics*, vol. 3, no. 3, pp. 165–171, 2020.

[23] S. Nie and I. F. Akyildiz, "Metasurfaces for multiplexed communication," *Nature Electronics*, vol. 4, no. 3, pp. 177-178, 2021.

[24] Y. Zhai, S. N. David, D. Zhao, R. Lou, G. Tan, and R. Yang, "Scalable-manufactured randomized glass-polymer hybrid metamaterial for daytime radiative cooling," *Science*, vol. 355, no. 6329, pp. 1062–1066, 2017.

[25] A. P. Raman, W. Li, A. P. Raman, W. Li, and S. Fan, "Generating Light from Darkness," *Joule*, vol. 3, no. 11, pp. 2679–2686, 2019.

[26] Y. Kwon, S. H. Song, J. C. Bae, A. Jo, M. Kwon, and S. H. Han, "Metasurface-driven OLED displays beyond 10,000 pixels per inch," *Science*, vol. 370, no. 6515, pp. 459–463, 2020.

[27] Y. Xie, P. Ni, Q. Wang et al., "Metasurface-integrated vertical cavity surface-emitting lasers for programmable directional lasing emissions," *Nature Nanotechnology*, vol. 15, no. 2, pp. 125–130, 2020.

[28] G. Lee, J. Hong, S. Hwang et al., "Metasurface eyepiece for augmented reality," *Nature Communications*, vol. 9, no. 1, p. 4562, 2018.

[29] J.-S. Park, S. Zhang, A. She et al., "All-glass, large metalens at visible wavelength using deep-ultraviolet projection lithography," *Nano Letters*, vol. 19, no. 12, pp. 8673–8682, 2019.

[30] S. Kang, Z. Qian, V. Rajaram, C. Cassella, N. E. McGruer, and M. Rinaldi, "Zero-power infrared digitizers based on plasmonically enhanced micromechanical photoswitches," *Nature Nanotechnology*, vol. 12, no. 10, pp. 969–973, 2017.

[31] X. Zhao, G. Duan, K. Wu, S. W. Anderson, and X. Zhang, "Intelligent metamaterials based on nonlinearity for magnetic resonance imaging," *Advanced Materials*, vol. 31, no. 49, article 1905461, 2019.

[32] C. Pfeiffer and A. Grbic, "Metamaterial Huygens' surfaces: tailoring wave fronts with reflectionless sheets," *Physical Review Letters*, vol. 110, no. 19, article 197401, 2013.

[33] X. Zhao, J. Schalch, J. Zhang et al., "Electromechanically tunable metasurface transmission waveplate at terahertz frequencies," *Optica*, vol. 5, no. 3, pp. 303–310, 2018.

[34] W. Zhuo, S. Sun, Q. He, and L. Zhou, "A review of high-efficiency Pancharatnam–Berry metasurfaces," *Terahertz Science and Technology*, vol. 13, no. 3, pp. 73–89, 2020.

[35] S. Sun, Q. He, S. Xiao, Q. Xu, X. Li, and L. Zhou, "Gradient-index meta-surfaces as a bridge linking propagating waves and surface waves," *Nature Materials*, vol. 11, no. 5, pp. 426–431, 2012.

[36] C. Longqing, P. Prakash, W. Yang et al., "Active multifunctional microelectromechanical system metadevices: applications in polarization control, wavefront deflection, and holograms," *Advanced Optical Materials*, vol. 5, article 1600716, 2016.

[37] W. Liu, Z. Li, H. Cheng et al., "Metasurface enabled wide-angle Fourier lens," *Advanced Materials*, vol. 30, no. 23, article 1706368, 2018.

[38] F. Costa and A. Monorchio, "Closed-form analysis of reflection losses in microstrip Reflectarray antennas," *IEEE Transactions on Antennas and Propagation*, vol. 60, no. 10, pp. 4650–4660, 2012.

[39] D. R. Smith, S. Schultz, P. Markoš, and C. M. Soukoulis, "Determination of effective permittivity and permeability of metamaterials from reflection and transmission coefficients," *Physical Review B*, vol. 65, no. 19, article 195104, 2002.

[40] H. X. Xu, S. Ma, W. Luo et al., "Aberration-free and functionality-switchable meta-lenses based on tunable metasurfaces," *Applied Physics Letters*, vol. 109, no. 19, article 193506, 2016.

[41] G. Duan, J. Schalch, X. Zhao et al., "A survey of theoretical models for terahertz electromagnetic metamaterial absorbers," *Sensors and Actuators A: Physical*, vol. 287, pp. 21–28, 2019.

[42] S. Fan, W. Suh, and J. D. Joannopoulos, "Temporal coupled-mode theory for the Fano resonance in optical resonators," *Journal of the Optical Society of America. A*, vol. 20, no. 3, pp. 569–572, 2003.

[43] X. Zhao, J. Zhang, K. Fan et al., "Real-Time Tunable Phase Response and Group Delay in Broadside Coupled split-ring Resonators," *Physical Review B*, vol. 99, no. 24, article 245111, 2019.

[44] X. Zhao, C. Chen, K. Kaj et al., "Terahertz investigation of bound states in the continuum of metallic metasurfaces," *Optica*, vol. 7, no. 11, pp. 1548–1554, 2020.

[45] C. Gigli, Q. Li, P. Chavel, G. Leo, M. L. Brongersma, and P. Lalanne, "Fundamental Limitations of Huygens' Metasurfaces for Optical Beam Shaping," *Laser & Photonics Reviews*, vol. 15, no. 8, article 2000448, 2021.

[46] P. Lalanne, W. Yan, K. Vynck, C. Sauvan, and J. Hugonin, "Light Interaction with Photonic and Plasmonic Resonances," *Laser & Photonics Reviews*, vol. 12, no. 5, article 1700113, 2018.

[47] S. Chang, X. Guo, and X. Ni, "Optical Metasurfaces: Progress and Applications," *Annual Review of Materials Research*, vol. 48, no. 1, pp. 279–302, 2018.

[48] A. She, S. Zhang, S. Shian, D. R. Clarke, and F. Capasso, "Large area metalenses: design , characterization, and mass manufacturing," *Optics Express*, vol. 26, no. 2, pp. 1573–1585, 2018.

[49] H. Cai, S. Srinivasan, D. A. Czaplewski et al., "Inverse design of metasurfaces with non-local interactions," *npj Computational Materials*, vol. 6, no. 1, p. 116, 2020.

[50] B. Yang, T. Liu, H. Guo, S. Xiao, and L. Zhou, "High-performance meta-devices based on multilayer meta-atoms: interplay between the number of layers and phase coverage," *Science Bulletin*, vol. 64, pp. 823–835, 2019.

[51] I. Staude, A. E. Miroshnichenko, M. Decker et al., "Tailoring Directional Scattering through Magnetic and Electric Resonances in Subwavelength Silicon Nanodisks," *ACS Nano*, vol. 7, no. 9, pp. 7824–7832, 2013.

[52] A. C. Overvig, S. Shrestha, S. C. Malek et al., "Dielectric metasurfaces for complete and independent control of the optical amplitude and phase," *Light: Science & Applications*, vol. 8, no. 1, p. 92, 2019.

[53] M. M. Salary and H. Mosallaei, "Tunable All-Dielectric Metasurfaces for Phase-Only Modulation of Transmitted Light Based on Quasi-bound States in the Continuum," *ACS Photonics*, vol. 7, no. 7, pp. 1813–1829, 2020.

[54] S. Sun, K. Yang, C. Wang et al., "High-Efficiency Broadband Anomalous Reflection by Gradient Meta-Surfaces," *Nano Letters*, vol. 12, no. 12, pp. 6223–6229, 2012.

[55] Y. Yang, W. Wang, P. Moitra, I. I. Kravchenko, D. P. Briggs, and J. Valentine, "Dielectric Meta-Reflectarray for Broadband Linear Polarization Conversion and Optical Vortex Generation," *Nano Letters*, vol. 14, no. 3, pp. 1394–1399, 2014.

[56] Z. Miao, Q. Wu, X. Li et al., "Widely Tunable Terahertz Phase Modulation with Gate-Controlled Graphene Metasurfaces," *Physical Review X*, vol. 5, no. 4, article 041027, 2015.

[57] N. I. Landy, S. Sajuyigbe, J. J. Mock, D. R. Smith, and W. J. Padilla, "Perfect metamaterial absorber," *Physical Review Letters*, vol. 100, no. 20, article 207402, 2008.

[58] X. Liu, K. Fan, I. V. Shadrivov, and W. J. Padilla, "Experimental realization of a terahertz all-dielectric metasurface absorber," *Optics Express*, vol. 25, no. 1, pp. 191–201, 2017.

[59] M. Decker, I. Staude, M. Falkner et al., "High-efficiency dielectric Huygens' surfaces," *Advanced Optical Materials*, vol. 3, no. 6, pp. 813–820, 2015.

[60] C. M. Watts, X. Liu, and W. J. Padilla, "Metamaterial Electromagnetic Wave Absorbers," *Advanced Materials*, vol. 24, no. 23, pp. OP98–OP120, 2012.

[61] S. J. Kim, J. Park, M. Esfandyarpour, E. F. Pecora, P. G. Kik, and M. L. Brongersma, "Superabsorbing, Artificial Metal Films Constructed from Semiconductor Nanoantennas," *Nano Letters*, vol. 16, no. 6, pp. 3801–3808, 2016.

[62] F. Alves, D. Grbovic, and G. Karunasiri, "Investigation of microelectromechanical systems bimaterial sensors with metamaterial absorbers for terahertz imaging," *Optical Engineering*, vol. 53, no. 9, article 097103, 2014.

[63] W. Li and J. Valentine, "Metamaterial Perfect Absorber Based Hot Electron Photodetection," *Nano Letters*, vol. 14, no. 6, pp. 3510–3514, 2014.

[64] A. Kodigala, T. Lepetit, Q. Gu, B. Bahari, Y. Fainman, and B. Kanté, "Lasing action from photonic bound states in continuum," *Nature*, vol. 541, no. 7636, pp. 196–199, 2017.

[65] N. I. Zheludev and Y. S. Kivshar, "From metamaterials to metadevices," *Nature Materials*, vol. 11, no. 11, pp. 917–924, 2012.

[66] J. Y. Dai, W. Tang, M. Z. Chen et al., "Wireless Communication Based on Information Metasurfaces," *IEEE Transactions on Microwave Theory and Techniques*, vol. 69, no. 3, pp. 1493–1510, 2021.

[67] Z. Chen, B. Guo, Y. Yang, and C. Cheng, "Metamaterials-based enhanced energy harvesting: A review," *Physica B: Condensed Matter*, vol. 438, pp. 1–8, 2014.

[68] S. Fan and W. Li, "Photonics and thermodynamics concepts in radiative cooling," *Nature Photonics*, vol. 16, no. 3, pp. 182–190, 2022.

[69] M. Khorasaninejad and F. Capasso, "Metalenses: Versatile multifunctional photonic components," *Science*, vol. 358, no. 6367, article eaam8100, 2017.

[70] M. L. Tseng, H. Hsiao, C. H. Chu et al., "Metalenses: advances and applications," *Advanced Optical Materials*, vol. 6, no. 18, p. 1800554, 2018.

[71] B. Li, W. Piyawattanametha, and Z. Qiu, "Metalens-based miniaturized optical systems," *Micromachines*, vol. 10, no. 5, p. 310, 2019.

[72] W. Liu, H. Cheng, J. Tian, and S. Chen, "Diffractive metalens: from fundamentals, practical applications to current trends," *Advances in Physics: X*, vol. 5, article 1742584, 2020.

[73] X. Zou, G. Zheng, Q. Yuan et al., "Imaging based on metalenses," *PhotoniX*, vol. 1, no. 1, pp. 1–24, 2020.

[74] G.-Y. Lee, J. Sung, and B. Lee, "Metasurface optics for imaging applications," *MRS Bulletin*, vol. 45, no. 3, pp. 202–209, 2020.

[75] S.-J. Kim, C. Kim, Y. Kim et al., "Dielectric Metalens: Properties and Three-Dimensional Imaging Applications," *Sensors*, vol. 21, no. 13, p. 4584, 2021.

[76] B. H. Chen, P. C. Wu, V.-C. Su et al., "GaN metalens for pixel-level full-color routing at visible light," *Nano Letters*, vol. 17, pp. 6345–6352, 2018.

[77] X. Chen, L. Huang, H. Mühlenbernd et al., "Dual-polarity plasmonic metalens for visible light," *Nature Communications*, vol. 3, article 10.1038/ncomms2207, p. 1198, 2012.

[78] W. T. Chen, A. Y. Zhu, M. Khorasaninejad, Z. Shi, V. Sanjeev, and F. Capasso, "Immersion meta-lenses at visible wavelengths for nanoscale imaging," *Nano Letters*, vol. 17, pp. 3188–3194, 2017.

[79] R. Paniagua-Dominguez, Y. F. Yu, E. Khaidarov et al., "A metalens with a near-unity numerical aperture," *Nano Letters*, vol. 18, no. 3, pp. 2124–2132, 2018.

[80] Z.-B. Fan, Z.-K. Shao, M.-Y. Xie et al., "Silicon nitride metalenses for close-to-one numerical aperture and wide-angle visible imaging," *Physical Review Applied*, vol. 10, no. 1, article 14005, 2018.

[81] H. Liang, Q. Lin, X. Xie et al., "Ultrahigh numerical aperture metalens at visible wavelengths," *Nano Letters*, vol. 18, no. 7, pp. 4460–4466, 2018.

[82] F. Aieta, P. Genevet, M. Kats, and F. Capasso, "Aberrations of flat lenses and aplanatic metasurfaces," *Optics Express*, vol. 21, no. 25, pp. 31530–31539, 2013.

[83] F. Aieta, P. Genevet, M. A. Kats et al., "Aberration-Free Ultrathin Flat Lenses and Axicons at Telecom Wavelengths Based on Plasmonic Metasurfaces," *Nano Letters*, vol. 12, no. 9, pp. 4932–4936, 2012.

[84] A. Arbabi, E. Arbabi, S. M. Kamali, Y. Horie, S. Han, and A. Faraon, "Miniature optical planar camera based on a wide-angle metasurface doublet corrected for monochromatic aberrations," *Nature Communications*, vol. 7, article 13682, 2016.

[85] B. Groever, W. T. Chen, and F. Capasso, "Meta-lens doublet in the visible region," *Nano Letters*, vol. 17, no. 8, pp. 4902–4907, 2017.

[86] M. Khorasaninejad, F. Aieta, P. Kanhaiya et al., "Achromatic metasurface lens at telecommunication wavelengths," *Nano Letters*, vol. 15, no. 8, pp. 5358–5362, 2015.

[87] F. Aieta, M. A. Kats, P. Genevet, and F. Capasso, "Multiwavelength achromatic metasurfaces by dispersive phase compensation," *Science*, vol. 347, no. 6228, pp. 1342–1345, 2015.

[88] E. Arbabi, A. Arbabi, S. M. Kamali, Y. Horie, and A. Faraon, "Multiwavelength metasurfaces through spatial multiplexing," *Scientific Reports*, vol. 6, no. 1, article 32803, 2016.

[89] S. Wang, P. C. Wu, V.-C. Su et al., "Broadband achromatic optical metasurface devices," *Nature Communications*, vol. 8, p. 187, 2017.

[90] E. Arbabi, A. Arbabi, S. M. Kamali, Y. Horie, and A. Faraon, "Controlling the sign of chromatic dispersion in diffractive optics with dielectric metasurfaces," *Optica*, vol. 4, no. 6, pp. 625–632, 2017.

[91] W. T. Chen, A. Y. Zhu, V. Sanjeev et al., "A broadband achromatic metalens for focusing and imaging in the visible," *Nature Nanotechnology*, vol. 13, no. 3, pp. 220–226, 2018.

[92] O. Avayu, E. Almeida, Y. Prior, and T. Ellenbogen, "Composite functional metasurfaces for multispectral achromatic optics," *Nature Communications*, vol. 8, article 14992, 2017.

[93] H. Li, X. Xiao, B. Fang et al., "Bandpass-filter-integrated multiwavelength achromatic metalens," *Photonics Research*, vol. 9, pp. 1384–1390, 2021.

[94] C. Kim, S.-J. Kim, and B. Lee, "Doublet metalens design for high numerical aperture and simultaneous correction of chromatic and monochromatic aberrations," *Optics Express*, vol. 28, no. 12, pp. 18059–18076, 2020.

[95] K. Ou, F. Yu, G. Li et al., "Broadband achromatic metalens in mid-wavelength infrared," *Laser & Photonics Reviews*, vol. 15, no. 9, article 2100020, 2021.

[96] K. Ou, F. Yu, G. Li et al., "Mid-infrared polarization-controlled broadband achromatic metadevice," *Science Advances*, vol. 6, no. 37, article eabc0711, 2020.

[97] H. Pahlevaninezhad, M. Khorasaninejad, Y.-W. Huang et al., "Nano-optic endoscope for high-resolution optical coherence tomography in vivo," *Nature Photonics*, vol. 12, no. 9, pp. 540–547, 2018.

[98] C. Chen, W. Song, J.-W. Chen et al., "Spectral tomographic imaging with aplanatic metalens," *Light: Science & Applications*, vol. 8, pp. 1–8, 2019.

[99] H.-Y. Qiu, Z.-B. Fan, H.-L. Zhang et al., "A broadband achromatic metalens array for integral imaging in the visible," *Light: Science & Applications*, vol. 8, p. 67, 2019.

[100] A. L. Holsteen, D. Lin, I. Kauvar, G. Wetzstein, and M. L. Brongersma, "A light-field metasurface for high-resolution single-particle tracking," *Nano Letters*, vol. 19, no. 4, pp. 2267–2271, 2019.

[101] R. J. Lin, V.-C. Su, S. Wang et al., "Achromatic metalens array for full-colour light-field imaging," *Nature Nanotechnology*, vol. 14, no. 3, pp. 227–231, 2019.

[102] Q. Guo, Z. Shi, Y.-W. Huang et al., "Compact single-shot metalens depth sensors inspired by eyes of jumping spiders," *Proceedings of the National Academy of Sciences*, vol. 116, no. 46, pp. 22959–22965, 2019.

[103] Z. Li, P. Lin, Y.-W. Huang et al., "Meta-optics achieves RGB-achromatic focusing for virtual reality," *Science Advances*, vol. 7, no. 5, article eabe4458, 2021.

[104] M. Khorasaninejad, W. T. Chen, A. Y. Zhu et al., "Multispectral chiral imaging with a metalens," *Nano Letters*, vol. 16, no. 7, pp. 4595–4600, 2016.

[105] E. Arbabi, S. M. Kamali, A. Arbabi, and A. Faraon, "Full-Stokes imaging polarimetry using dielectric metasurfaces," *ACS Photonics*, vol. 5, no. 8, pp. 3132–3140, 2018.

[106] F. Zhao, R. Lu, X. Chen et al., "Metalens-Assisted System for Underwater Imaging," *Laser & Photonics Reviews*, vol. 15, no. 8, article 2100097, 2021.

[107] S. Zhang, A. Soibel, S. A. Keo et al., "Solid-immersion metalenses for infrared focal plane arrays," *Applied Physics Letters*, vol. 113, no. 11, article 111104, 2018.

[108] O. Akın and H. V. Demir, "Mid-wave infrared metasurface microlensed focal plane array for optical crosstalk suppression," *Optics Express*, vol. 23, no. 21, pp. 27020–27027, 2015.

[109] S. H. Hwang, J. Cho, S. Jeon et al., "Gold-nanocluster-assisted nanotransfer printing method for metasurface hologram fabrication," *Scientific Reports*, vol. 9, p. 3051, 2019.

[110] J. Y. Suen, K. Fan, J. Montoya et al., "Multifunctional metamaterial pyroelectric infrared detectors," *Optica*, vol. 4, pp. 276–279, 2017.

[111] Y. Ni, S. Chen, Y. Wang, Q. Tan, S. Xiao, and Y. Yang, "Metasurface for structured light projection over 120° field of view," *Nano Letters*, vol. 20, no. 9, pp. 6719–6724, 2020.

[112] P. Mao, C. Liu, X. Li et al., "Single-step-fabricated disordered metasurfaces for enhanced light extraction from LEDs," *Light: Science & Applications*, vol. 10, p. 180, 2021.

[113] G. Rosolen, L. J. Wong, N. Rivera, B. Maes, M. Soljačić, and I. Kaminer, "Metasurface-based multi-harmonic free-electron light source," *Light: Science & Applications*, vol. 7, p. 64, 2018.

[114] M. Semmlinger, M. L. Tseng, J. Yang et al., "Vacuum ultraviolet light-generating metasurface," *Nano Letters*, vol. 18, no. 9, pp. 5738–5743, 2018.

[115] X. Liu, T. Tyler, T. Starr, A. F. Starr, N. M. Jokerst, and W. J. Padilla, "Taming the blackbody with infrared metamaterials as selective thermal emitters," *Physical Review Letters*, vol. 107, no. 4, article 045901, 2011.

[116] T. Cao, X. Zhang, W. Dong et al., "Tuneable thermal emission using chalcogenide metasurface," *Advanced Optical Materials*, vol. 6, no. 16, article 1800169, 2018.

[117] L. Liu, T. Li, Z. Liu et al., "Terahertz polarization sensing based on metasurface microsensor display anti-proliferation of tumor cells with aspirin," *Optics Express*, vol. 11, no. 5, pp. 2416–2430, 2020.

[118] H. Leonard, S. Halachmi, N. Ben-Dov, O. Nativ, and E. Segal, "Unraveling Antimicrobial Susceptibility of Bacterial Networks on Micropillar Architectures Using Intrinsic Phase-Shift Spectroscopy," *ACS Nano*, vol. 11, no. 6, pp. 6167–6177, 2017.

[119] K. Chen, T. D. Dao, S. Ishii, M. Aono, and T. Nagao, "Infrared aluminum metamaterial perfect absorbers for plasmon-enhanced infrared spectroscopy," *Advanced Functional Materials*, vol. 25, no. 42, pp. 6637–6643, 2015.

[120] D. Li, H. Zhou, X. Hui, X. He, and X. Mu, "Plasmonic Biosensor Augmented by a Genetic Algorithm for Ultra-Rapid, Label-Free, and Multi-Functional Detection of COVID-19," *Analytical Chemistry*, vol. 93, no. 27, pp. 9437–9444, 2021.

[121] Y. Wang, M. A. Ali, E. K. C. Chow, L. Dong, and M. Lu, "An optofluidic metasurface for lateral flow-through detection of breast cancer biomarker," *Biosensors & Bioelectronics*, vol. 107, pp. 224–229, 2018.

[122] H. Zhou, X. Hui, D. Li et al., "Metal–organic framework-surface-enhanced infrared absorption platform enables simultaneous on-chip sensing of greenhouse gases," *Advanced Science*, vol. 7, article 2001173, 2020.

[123] Y. Wang, Z. Cui, X. Zhang et al., "Excitation of Surface Plasmon Resonance on Multiwalled Carbon Nanotube Metasurfaces for Pesticide Sensors," *ACS Applied Materials & Interfaces*, vol. 12, no. 46, pp. 52082–52088, 2020.

[124] J. Gao, N. Zhang, D. Ji et al., "Superabsorbing Metasurfaces with Hybrid Ag–Au Nanostructures for Surface-Enhanced Raman Spectroscopy Sensing of Drugs and Chemicals," *Small Methods*, vol. 2, no. 7, article 1800045, 2018.

[125] X. Tan, H. Zhang, J. Li et al., "Non-dispersive infrared multi-gas sensing via nanoantenna integrated narrowband detectors," *Nature Communications*, vol. 11, no. 1, p. 5245, 2020.

[126] W. J. Padilla, M. T. Aronsson, C. Highstrete, M. Lee, A. J. Taylor, and R. D. Averitt, "Electrically resonant terahertz metamaterials: Theoretical and experimental investigations," *Physical Review B*, vol. 75, no. 4, article 41102, 2007.

[127] D. R. Smith, D. C. Vier, N. Kroll, and S. Schultz, "Direct calculation of permeability and permittivity for a left-handed metamaterial," *Applied Physics Letters*, vol. 77, no. 14, pp. 2246–2248, 2000.

[128] V. A. Fedotov, M. Rose, S. L. Prosvirnin, N. Papasimakis, and N. I. Zheludev, "Sharp trapped-mode resonances in planar metamaterials with a broken structural symmetry," *Physical Review Letters*, vol. 99, no. 14, article 147401, 2007.

[129] C. P. Ho, P. Pitchappa, and C. Lee, "Digitally reconfigurable binary coded terahertz metamaterial with output analogous to NOR and AND," *Applied Physics Letters*, vol. 119, no. 15, article 153104, 2016.

[130] M. Manjappa, P. Pitchappa, N. Singh et al., "Reconfigurable MEMS Fano metasurfaces with multiple-input-output states for logic operations at terahertz frequencies," *Nature Communications*, vol. 9, no. 1, p. 4056, 2018.

[131] M. Liu, M. Susli, D. Silva et al., "Ultrathin tunable terahertz absorber based on MEMS-driven metamaterial," *Microsystems & Nanoengineering*, vol. 3, no. 1, p. 17033, 2017.

[132] J. Kappa, D. Sokoluk, S. Klingel, C. Shemelya, E. Oesterschulze, and M. Rahm, "Electrically Reconfigurable Micromirror Array for Direct Spatial Light Modulation of Terahertz Waves over a Bandwidth Wider Than 1 THz," *Scientific Reports*, vol. 9, no. 1, p. 2597, 2019.

[133] K. Chen, Y. Feng, F. Monticone et al., "A Reconfigurable Active Huygens' Metalens," *Advanced Materials*, vol. 29, no. 17, article 1606422, 2017.

[134] T. J. Cui, M. Q. Qi, X. Wan, J. Zhao, and Q. Cheng, "Coding metamaterials, digital metamaterials and programmable metamaterials," *Light: Science & Applications*, vol. 3, no. 10, pp. e218–e218, 2014.

[135] T. Cui, L. Li, S. Liu et al., "Information Metamaterial Systems," *iScience*, vol. 23, no. 8, article 101403, 2020.

[136] S. Li, X. Xu, R. M. Veetil, V. Valuckas, R. Paniagua-Domiguez, and A. I. Kuznetsov, "Phase-only transmissive spatial light modulator based on tunable dielectric metasurface," *Science*, vol. 364, no. 6445, pp. 1087–1090, 2019.

[137] X. Yin, T. Steinle, L. Huang et al., "Beam switching and bifocal zoom lensing using active plasmonic metasurfaces," *Light: Science & Applications*, vol. 6, no. 7, article e17016, 2017.

[138] Y. Yao, R. Shankar, M. A. Kats et al., "Electrically tunable metasurface perfect absorbers for ultrathin mid-infrared optical modulators," *Nano Letters*, vol. 14, no. 11, pp. 6526–6532, 2014.

[139] H. Lin, B. C. P. Sturmberg, K. Te Lin et al., "A 90-nm-thick graphene metamaterial for strong and extremely broadband absorption of unpolarized light," *Nature Photonics*, vol. 13, no. 4, pp. 270–276, 2019.

[140] J. van de Groep, J. H. Song, U. Celano, Q. Li, P. G. Kik, and M. L. Brongersma, "Exciton resonance tuning of an atomically thin lens," *Nature Photonics*, vol. 14, no. 7, pp. 426–430, 2020.

[141] Y. Zhang, C. Fowler, J. Liang et al., "Electrically reconfigurable non-volatile metasurface using low-loss optical phase-change material," *Nature Nanotechnology*, vol. 16, no. 6, pp. 661–666, 2021.

[142] Y. Wang, P. Landreman, D. Schoen et al., "Electrical tuning of phase-change antennas and metasurfaces," *Nature Nanotechnology*, vol. 16, no. 6, pp. 667–672, 2021.

[143] J. Park, B. G. Jeong, S. Il Kim et al., "All-solid-state spatial light modulator with independent phase and amplitude control for three-dimensional LiDAR applications," *Nature Nanotechnology*, vol. 16, no. 1, pp. 69–76, 2021.

[144] G. K. Shirmanesh, R. Sokhoyan, R. A. Pala, and H. A. Atwater, "Dual-Gated Active Metasurface at 1550 nm with Wide (>300°) Phase Tunability," *Nano Letters*, vol. 18, no. 5, pp. 2957–2963, 2018.

[145] C. M. Watt, D. Shrekenhamer, J. Montoya et al., "Terahertz compressive imaging with metamaterial spatial light modulators," *Nature Photonics*, vol. 8, no. 8, pp. 605–609, 2014.

[146] W. Li, X. Hu, J. Wu et al., "Dual-color terahertz spatial light modulator for single-pixel imaging," *Light: Science & Applications*, vol. 11, no. 1, p. 191, 2022.

[147] W. J. Padilla and R. D. Averitt, "Imaging with metamaterials," *Nature Reviews Physics*, vol. 4, no. 2, pp. 85–100, 2022.

[148] Y. Chang, J. Wei, and C. Lee, "Metamaterials-From fundamentals and MEMS tuning mechanisms to applications," *Nanophotonics*, vol. 9, no. 10, pp. 3049–3070, 2020.

[149] Q. He, S. Sun, and L. Zhou, "Tunable/Reconfigurable Metasurfaces: Physics and Applications," *Research*, vol. 2019, article 1849272, pp. 1–16, 2019.

[150] X. Zhao, G. Duan, A. Li, C. Chen, and X. Zhang, "Integrating microsystems with metamaterials towards metadevices," *Microsystems & Nanoengineering*, vol. 5, no. 1, p. 5, 2019.

[151] H. Tao, A. C. Strikwerda, K. Fan, W. J. Padilla, X. Zhang, and R. D. Averitt, "Reconfigurable terahertz metamaterials," *Physical Review Letters*, vol. 103, no. 14, article 147401, 2009.

[152] P. Pitchappa, C. P. Ho, L. Dhakar, and C. Lee, "Microelectromechanically reconfigurable interpixelated metamaterial for independent tuning of multiple resonances at terahertz spectral region," *Optica*, vol. 2, no. 6, p. 571, 2015.

[153] L. Cong, P. Pitchappa, C. Lee, and R. Singh, "Active Phase Transition via Loss Engineering in a Terahertz MEMS Metamaterial," *Advanced Materials*, vol. 29, no. 26, article 1700733, 2017.

[154] W. M. Zhu, A. Q. Liu, T. Bourouina et al., "Microelectromechanical Maltese-cross metamaterial with tunable terahertz anisotropy," *Nature Communications*, vol. 3, no. 1, p. 1274, 2012.

[155] R. Pan, Z. Liu, W. Zhu, S. Du, C. Gu, and J. Li, "Asymmetrical Chirality in 3D Bended Metasurface," *Advanced Functional Materials*, vol. 31, no. 31, article 2100689, 2021.

[156] P. Pitchappa, A. Kumar, H. Liang et al., "Frequency-Agile Temporal Terahertz Metamaterials," *Advanced Optical Materials*, vol. 8, no. 12, article 2000101, 2020.

[157] T. Shimura, T. Kinoshita, Y. Koto, N. Umeda, and K. Iwami, "Birefringent reconfigurable metasurface at visible wavelengths by MEMS nanograting," *Applied Physics Letters*, vol. 113, no. 17, article 171905, 2018.

[158] A. C. Strikwerda, K. Fan, H. Tao, D. V. Pilon, X. Zhang, and R. D. Averitt, "Comparison of birefringent electric split-ring resonator and meanderline structures as quarter-wave plates at terahertz frequencies," *Optics Express*, vol. 17, no. 1, pp. 136–149, 2009.

[159] J. Hao, Y. Yuan, L. Ran et al., "Manipulating electromagnetic wave polarizations by anisotropic metamaterials," *Physical Review Letters*, vol. 99, article 063908, 2007.

[160] T. Kan, A. Isozaki, N. Kanda et al., "Enantiomeric switching of chiral metamaterial for terahertz polarization modulation employing vertically deformable MEMS spirals," *Nature Communications*, vol. 6, no. 1, p. 8422, 2015.

[161] N. A. Rubin, G. D'Aversa, P. Chevalier, Z. Shi, W. T. Chen, and F. Capasso, "Matrix Fourier optics enables a compact full-Stokes polarization camera," *Science*, vol. 365, no. 6448, 2019.

[162] H. Q. Nguyen, B. C. Baxter, K. Brower et al., "Programmable Microfluidic Synthesis of Over One Thousand Uniquely Identifiable Spectral Codes," *Advanced Optical Materials*, vol. 5, no. 3, 2017.

[163] J. Rogers, Y. Huang, O. G. Schmidt, and D. H. Gracias, "Origami MEMS and NEMS," *MRS Bulletin*, vol. 41, no. 2, pp. 123–129, 2016.

[164] J. Li and Z. Liu, "Focused-ion-beam-based nano-kirigami: From art to photonics," *Nanophotonics*, vol. 7, no. 10, pp. 1637–1650, 2018.

[165] Q. Wang, D. Mao, P. Liu, T. Koschny, C. M. Soukoulis, and L. Dong, "NEMS-Based Infrared Metamaterial via Tuning Nanocantilevers Within Complementary Split Ring Resonators," *Journal of Microelectromechanical Systems*, vol. 26, no. 6, pp. 1371–1380, 2017.

[166] S. Chen, W. Wei, Z. Liu et al., "Reconfigurable nano-kirigami metasurfaces by pneumatic pressure," *Photonics Research*, vol. 8, no. 7, p. 1177, 2020.

[167] Z. Liu, H. Du, J. Li, L. Lu, Z.-Y. Li, and N. X. Fang, "Nano-kirigami with giant optical chirality," *Science Advances*, vol. 4, no. 7, article eaat4436, 2018.

[168] L. Jing, Z. Wang, K. Yao et al., "Origami-Based Reconfigurable Metamaterials for Tunable Chirality," *Advanced Materials*, vol. 29, article 1700412, 2017.

[169] S. Chen, Z. Liu, H. Du et al., "Electromechanically reconfigurable optical nano-kirigami," *Nature Communications*, vol. 12, p. 1229, 2021.

[170] Y. Han, S. Chen, C. Ji et al., "Reprogrammable optical metasurfaces by electromechanical reconfiguration," *Optics Express*, vol. 29, no. 19, pp. 30751–30760, 2021.

[171] A. L. Holsteen, A. F. Cihan, and M. L. Brongersma, "Temporal color mixing and dynamic beam shaping with silicon metasurfaces," *Science*, vol. 365, no. 6450, pp. 257–260, 2019.

[172] C. Meng, P. C. V. Thrane, F. Ding et al., "Dynamic piezoelectric MEMS-based optical metasurfaces," *Science Advances*, vol. 7, pp. 5639–5662, 2021.

[173] E. Arbabi, A. Arbabi, S. M. Kamali, Y. Horie, M. S. Faraji-Dana, and A. Faraon, "MEMS-tunable dielectric metasurface lens," *Nature Communications*, vol. 9, no. 1, p. 812, 2018.

[174] Z. Han, S. Colburn, A. Majumdar, and K. F. Böhringer, "MEMS-actuated metasurface Alvarez lens," *Microsystems & Nanoengineering*, vol. 6, no. 1, p. 79, 2020.

[175] A. Pors and S. I. Bozhevolnyi, "Plasmonic metasurfaces for efficient phase control in reflection," *Optics Express*, vol. 21, no. 22, pp. 27438–27451, 2013.

[176] A. Pors, O. Albrektsen, I. P. Radko, and S. I. Bozhevolnyi, "Gap plasmon-based metasurfaces for total control of reflected light," *Scientific Reports*, vol. 3, no. 1, p. 2155, 2013.

[177] T. Roy, S. Zhang, I. W. Jung, M. Troccoli, F. Capasso, and D. Lopez, "Dynamic metasurface lens based on MEMS technology," *APL Photonics*, vol. 3, no. 2, article 21302, 2018.

[178] G. Zhou, H. Yu, and F. S. Chau, "Microelectromechanically-driven miniature adaptive Alvarez lens," *Optics Express*, vol. 21, no. 1, pp. 1226–1233, 2013.

[179] Y. Zou, W. Zhang, F. S. Chau, and G. Zhou, "Miniature adjustable-focus endoscope with a solid electrically tunable lens," *Optics Express*, vol. 23, no. 16, article 20582, 2015.

[180] S. Colburn, A. Zhan, and A. Majumdar, "Varifocal zoom imaging with large area focal length adjustable metalenses," *Optica*, vol. 5, no. 7, pp. 825–831, 2018.

[181] A. Zhan, S. Colburn, C. M. Dodson, and A. Majumdar, "Metasurface freeform nanophotonics," *Scientific Reports*, vol. 7, article 1673, 2017.

[182] V. Bansal and P. Saggau, "Digital Micromirror Devices: Principles and Applications in Imaging," *Cold Spring Harbor Protocols*, vol. 2013, article 074302, 2013.